Boron nitride nanotubes supported icosahedral Pd nanoparticles: Enabling ultrahigh current density-superior hydrogen evolution activity and theoretical insights

Sada Venkateswarlu [a,1], Sooyeon Kim [b,1], Mani Balamurugan [c], Younghu Son [d], Minyoung Yoon [d], Ki Tae Nam [c], Sang Soo Han [b,*], Myung Jong Kim [a,*]

[a] Department of Chemistry, Gachon University, Seongnam 13120, Republic of Korea
[b] Computational Science Research Center, Korea Institute of Science and Technology (KIST), Seoul 02792, Republic of Korea
[c] Department of Materials Science and Engineering, Seoul National University (SNU), 1 Gwanak ro, Seoul 08826, Republic of Korea
[d] Department of Chemistry, Kyungpook National University (KNU), Daegu 41566, Republic of Korea

ARTICLE INFO

ABSTRACT

An in-situ growth of icosahedral (IC) Pd nanoparticles (NPs) on boron nitride nanotubes (BNNTs) is explored with an external surfactant and reducing agent-free strategy. The IC-Pd@BNNT catalysts show an ultrahigh current density of over -1000 mA cm^{-2} with a low overpotential of 199 mV for the hydrogen evolution reaction (HER). At -20 mA cm^{-2}, the overpotential was as low as 15.7 mV in an acidic medium, which is superior than commercial Pd/C (62.6 mV), and Pt/C (29.4 mV). Moreover, the HER activity of the IC-Pd@BNNT catalysts is maintained even after an accelerated durability test of 40,000 cycles, indicating that the BNNTs are served as a durable support, maintaining the structural integrity of the catalyst. Density functional theory (DFT) calculations confirm that the IC-Pd on the BNNT support with vacancy defects is highly stable and HER active. From the Gas chromatography H$_2$ gas was quantified, and the Faradaic efficiency was achieved to 98.96%.

1. Introduction

The rapid growth in industrialization, transportation, and e-technology has resulted in escalating energy consumption, fossil fuel depletion, and global warming, which calls for advanced, versatile electrochemical energy conversion and storage technologies [1,2]. Water is a primary renewable resource, and electrochemical water splitting is one of the main technologies used to produce hydrogen fuel, an alternate energy source to fossil fuels [3,4]. Thus far, Pt has been considered the benchmark cathode catalyst for hydrogen evolution reactions (HERs) [5]; however, its use has been limited owing to its natural scarcity and high capital cost [6]. Pd can be considered a potential substitute for Pt in HER catalysis because of its availability, extensive use in automotive catalytic converters, organic catalysis (Suzuki reaction) and excellent host for hydrogen (H) absorption and desorption [7–9]. The catalytic activity of noble metal nanoparticles (NPs) depends on physicochemical properties such as size, shape, and composition [8]. These metals often form cubes, cuboctahedrons, tetrahedrons,

octahedrons, and multi-twinned particles (MTPs) such as decahedra and icosahedra [10]. Owing to its 12 vertices, 30 edges covered by twin boundaries, and 20 faces, compressive strains of icosahedral NPs have been reported as impressive active catalysts [11]. Studies on the performance of icosahedral Pd bimetallic NPs such as Pd–Pt, Pd–Au, Pd–Ni, Pd–Fe, and Pd–Cu, as catalysts have shown excellent catalytic activity during ethanol electrooxidation, oxygen reduction reaction (ORR), and CO$_2$ reduction [12–16].

Carbon-allotrope materials, such as carbon nanotubes (CNT) and reduced graphene oxides supported NPs, are well-known electrochemical conductive support materials used in energy conversion and storage due to their outstanding conductivity [17]. Recently, the implementation of Pd NPs with various carbon substrates, such as carbon fibers, CNTs, graphene, and activated carbon, as catalysts in HER was successful [18–20]. However, the thermodynamic instability of carbon materials results in their oxidization at higher overpotentials, leading to the destruction of the structural integrity of the catalyst and subsequent agglomeration of NPs, hindering catalytic activity,

---

especially over prolonged periods [21–23]. Therefore, introducing an effective ultra-durable electrochemical catalyst to mitigate these effects is of great importance. The boron nitride nanotubes (BNNTs) have similar structural features to that of CNT. In addition, BNNTs has several outstanding features such as ultra-high thermal conductivity, tunability, wide bandgap, super hydrophobicity, durable chemical stability (including oxidation and corrosion resistance) in harsh conditions, piezoelectricity, hydrogen storage capacity and blocking thermal neutrons, local dipole moments, and ionic character due to electronegative differences, are highly desirable in fields such as electronics, optometry, space technology, and material science. Despite the many advantages of BNNTs, their implementation in electrochemical catalysis support material for energy conversion and storage at an industrial scale is yet to be attained owing to its wide bandgap (>4.5 eV) and because it acts as an insulator, which is electrochemically inactive [24–27]. Recently, a few studies have successfully implemented carbon-intercalated two-dimensional (2D) h-BN materials as electrochemical catalytic support [28–32]. This represents a significant opportunity for the development of BNNTs as a robust electrochemical catalyst. To the best of the authors' knowledge, no BNNTs have been used as experimental electrochemical catalytic supports during HERs. Therefore, this study aims to develop icosahedral Pd NPs anchored onto defective sites with BNNT (IC-Pd@BNNT), which act as excellent multifunctional substrates for electrochemical HERs that can compete with commercial Pt/C.

2. Experimental section

2.1. Purification of BN nanotubes (BNNTs)

450 mg of BNNT-SP10 puffballs (purchased from BNNT LLC) were placed into a ceramic crucible and heated at 650 °C for 6 h using a muffle furnace, then cooled to room temperature (22 °C). After this process, the color of BNNT changed from light ash to white (Scheme 1). Subsequently, the calcinated BNNTs were dispersed in 500 mL of deionized water (DI) and stirred at a speed of 1450 rpm for up to 3 h. The reaction solution was then suction filtered through a Whatman no. 41 filter paper, and the residue was washed several times using methanol and hot water. The washed BNNTs were then dried in an oven at 80 °C for 12 h.

2.2. Synthesis of IC-Pd@BNNTs

60 mg of Palladium (II) chloride (PdCl$_2$) was added to 40 mL of DMF solution in a 50 mL glass vial and sonicated for 20 min. Subsequently, 100 mg of purified BNNTs were added, and the solution was sonicated at 50 °C for 90 min. The reaction mixture was transferred into a Teflon-lined stainless-steel autoclave and kept at 125 °C for 30 h. Afterward, the sample was centrifuged and washed one time with DMF, and three times using methanol, and DI water to obtain the IC-Pd@BNNT catalyst, which was then stored in a closed vial at room temperature (22 °C). In addition to 60 mg of PdCl$_2$, for comparison of the concentration of Pd loading on BNNT we have taken 30 mg and 100 mg of PdCl$_2$ precursor for the synthesis of IC-Pd@BNNT (30 mg) and IC-Pd@BNNT (100 mg) respectively (30 mg, 60 mg, 100 mg names as low (L), medium (M) and high (H) concentrations of Pd). Bare Pd NPs were also synthesized using the same procedure in the absence of BNNT. Additionally, a Pd@CN catalyst was synthesized using the previously described procedure but with 2D carbon nitrogen sheets derived from the pyrolysis of EDTA at high temperatures (1000 °C) in an N$_2$ medium replacing BNNT.

2.3. Electrochemical measurements

Electrochemical analysis of the IC-Pd@BNNT catalyst was performed using a standard three-electrode cell system in 0.5 M H$_2$SO$_4$ after purging N$_2$ gas for 15 min at room temperature using a Biologic SP-200
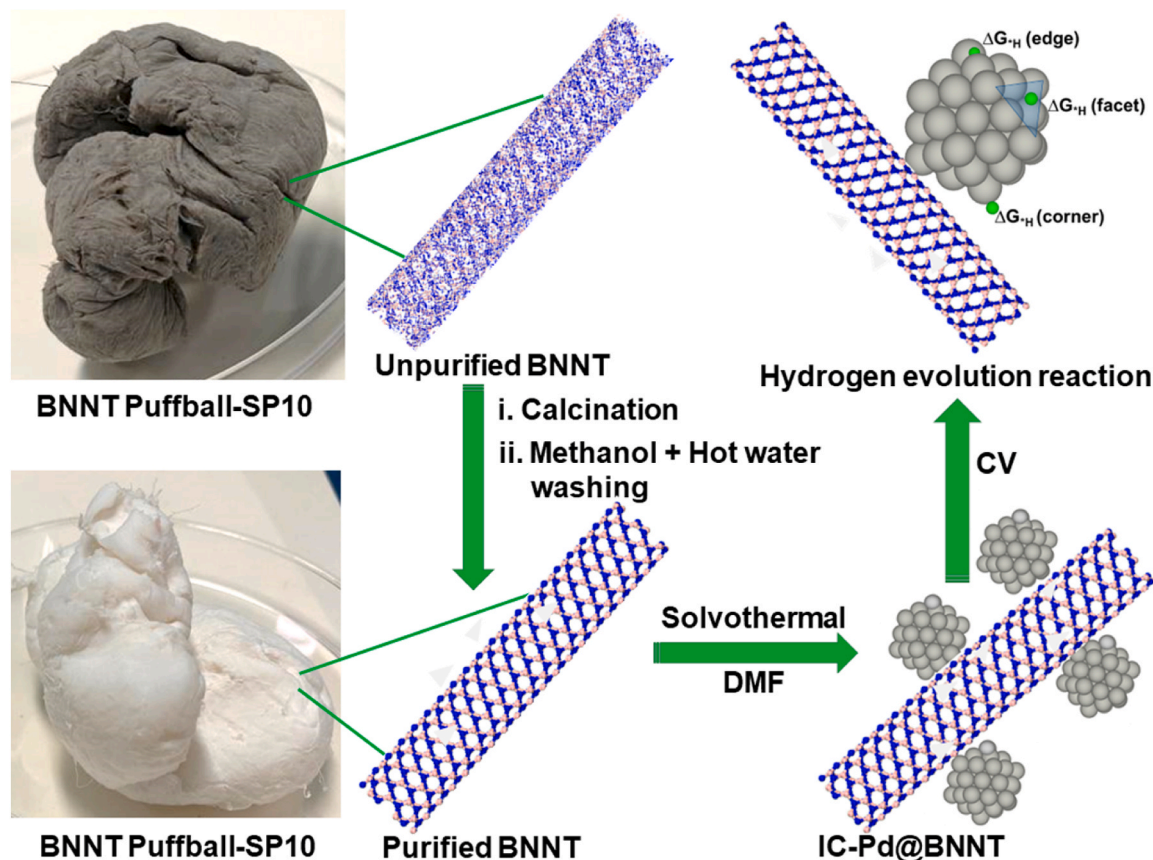
Scheme 1. Schematic illustration of the purification of pristine BNNT, the synthesis of IC-Pd@BNNT, and its hydrogen evolution reaction.

electrochemical workstation. In this system, carbon paper was used as the working electrode. The edge of the carbon paper (CP) was connected to a copper wire using a silver paste, and the electrical contact was sealed with an epoxy resin such that it exposed 0.25 cm² of carbon paper as the working area. Pt and Ag/AgCl wires were used as the counter electrode and reference electrode, respectively. The working electrode was prepared by mixing 2 mg of the IC-Pd@BNNT catalyst with 100 μL of deionized water, 600 μL of ethanol, and 300 μL of Nafion, followed by ultrasonication for 60 min to obtain a homogenized ink solution. This mixture was drop cast on the carbon paper surface before drying with a hot air gun. The loading mass of the catalyst on carbon paper was

$$TOF = \frac{J \times N_A}{2 \times F \times \Gamma} \tag{5}$$

J is the current density (mA cm⁻²), N_A is Avogadro's constant (6.022 ×10²³), F is the Faraday constant (96,485 C mol⁻¹), and Γ is the surface concentration of active sites.

2.3.2. Mass activity

The mass activity of the electrocatalysts was calculated as follows [34]:

$$mass \quad activity \quad \left(\frac{A}{mg_{Pd}}\right) = \frac{current \quad density(\frac{mA}{cm^2})}{sample \quad loading \quad on \quad electrode \quad surface\left(\frac{mg}{cm^2}\right) \times Pd \quad content \quad of \quad catalyst \quad (\%) \quad from \quad ICP-MS \times 1000} \tag{6}$$

0.35 mg cm⁻² (ICP-MS the Pd is (18.3 wt%)). Due to presence of BNNT support the active surface of the working electrode was activated by performing twice 500 CV cycles at a scan rate of 100 mV s⁻¹ using a cyclic voltammetry (CV) technique. The same working electrode was used for the linear sweep voltammogram (LSV) analysis at a scan rate of 2 mV s⁻¹. Tafel plots were constructed using the IR drop counter-balanced LSV curves. A stability test was performed by the chronoamperometry technique under 0.5 M H₂SO₄ (without IR compensation) at a current density of −100, −500, and −1000 mA cm⁻². The durability of the IC-Pd@BNNT catalysts was tested by repeating an LSV run every 10,000 cycles up to 40000 cycles at a scan rate of 100 mV s⁻¹ under 0.5 M H₂SO₄. Electrochemical impedance spectroscopy (EIS) was performed between frequencies ranging from 100 kHz to 0.1 Hz with an amplitude of 10 mV. Further, to optimize the HER activity of IC-Pd@BNNT catalyst we have tested the effect of various concentrations of Pd metal on BNNT (ICP-MS the Pd is 11.5 wt% and 29.4 wt%). The Ag/AgCl electrode was calibrated with respect to the reversible hydrogen electrode (RHE) as follows:

$$E_{RHE} = E_{Ag/AgCl} + 0·197 + 0·059 \times pH \tag{1}$$

The electrochemical active specific surface area (ECSA) was calculated as follows:

$$S_{ESCA} = \frac{C_{dl}}{C_s} \tag{2}$$

where C_{dl} represents the double-layer capacitance of electrode electrolyte interaction, and C_s is the specific capacitance (0.040 mF cm⁻²). The roughness factor (RF) was calculated as follows:

RF = ECSA/geometric area of the electrode, where the electrode geometric area is 0.25 cm².

Normalization calculations, such as the current density, were normalized based on the ESCA and Brunauer-Emmett- Teller (BET surface) as follows:

$$J_{ESCA} = J_O \times S_{ESCA}^{-1} \tag{3}$$

$$J_{BET} = J_O \times d^{-1} \times S_{BET}^{-1} \tag{4}$$

J_{ESCA} is the current density normalized by ECSA, J_{BET} is the current density normalized by BET surface area, J_o is the current density per unit area (mA cm⁻²), and d is the mass per unit area of the electrode on carbon paper (mg cm⁻²).

2.3.1. TOF

The TOF was calculated as follows [33]:

2.3.3. Specific activity

The specific activity of the electrocatalysts was calculated as follows [35]:

$$mass \quad activity \quad \left(\frac{mA}{cm_{ECSA}^2}\right) = \frac{mass \quad activity(\frac{mA}{mg_{catalyst}})}{ECSA(\frac{cm^2}{mg_{catalyst}})} \tag{7}$$

2.3.4. Number of active sites

The number of active sites was calculated as follows:

$$Number \quad active \quad sites = wt.\% \times loading \quad amount \times \frac{1mmol}{MW}$$
$$\times N_A \quad sites \quad mmol^{-1} \tag{8}$$

wt% is the metal weight of the metal in the catalyst, MW is the molecular weight, and N_A is Avogadro's constant.

The calculated number of active sites for IC-Pd@BNNTs was 35.87 × 10¹⁶ sites cm⁻².

2.4. Gas chromatography

To quantify the H₂ gas product quantities, a gas chromatograph (GC) equipped with a thermal conductivity detector (TCD) and a flame ionization detector (FID) (PerkinElmer, NARL8502 model 4003) was used. An H-cell with a three-electrode configuration was used for the electrochemical production of H₂ gas. Before performing the experiment, the H-cell was purged with N₂ gas to remove unwanted moisture in the cell. The working and counter (Pt) electrodes of this system were separated by a Nafion 117 membrane, and Ag/AgCl was used as the reference electrode. After bulk electrolysis (0.5 M H₂SO₄), 0.1 mL of gas was collected from the headspace of the electrochemical cell by using a Hamilton Gastight 1001 series micro syringe (1000 μL, USA) and injecting the gas into the GC. The gaseous products were separated using the Hayesep N and Molesieve 13X columns, and TCD was used to detect hydrogen, oxygen, and nitrogen. The number of moles of hydrogen was calculated using the area of the peaks—which were calibrated using a standard gas (0.1 mol%)—and headspace volume. All FE values represent an average of three runs.

2.5. Computational details

First-principles calculations were performed using the Vienna Ab initio Simulation Package (VASP) [36,37]. Projector augmented-wave (PAW) potentials [38] with a kinetic energy cutoff of 500 eV were

used to describe the core-valence electron interactions. Electronic exchange and correlations were described using the generalized gradient approximation (GGA) of the revised Perdew–Burke–Ernzerhof (RPBE) functional [39]. All atoms were fully relaxed, with a convergence criterion of 10^{-6} eV for the electronic self-consistent iteration and 0.03 eV/Å for the ionic iterations. Gaussian smearing of 0.10 eV was used to determine the electronic occupancies, and the spins were unrestricted. The Brillouin zone was sampled using a $3 \times 3 \times 1$ k-point mesh. The DFT-D3 method of Grimme et al. [40] was used for van der Waals (vdW) corrections, and dipole corrections were considered along the z-axis. Solvation effect was considered using the implicit solvent model ($\varepsilon = 78.5$) implemented in VASPsol.

For DFT calculations, Pd NPs were modeled with the icosahedral Pd_{13} structure. The magic number of atoms in IC-Pd NPs is 13, 55, 147, 309, 561, 923, etc. The size of the Pd NPs synthesized in this work is ~20 nm, indicating that the NPs consist of ~150,000 atoms (Fig. S37). Thus, based on the fact that an IC NP structure exposes only (111) facets, the Pd(111) slab structure would be a more representative model for the synthesized IC-Pd NPs than the small-sized Pd NP structures such as Pd_{13}

or Pd_{55}. However, in this work, Pd_{13} was mainly used to effectively explore how the support materials (e.g., BNNTs) interact with Pd NPs to enhance the HER catalytic activity. Pd_{55} and Pd(111) were also examined to investigate the size effect, and we found that the adsorption of H atoms become weaker for the larger Pd facets (Fig. S38-39), indicating that the HER activity can be increased with the size of the NPs. However, the trend of HER activity would not change (Fig. S40) as described in previous studies [41,42]. This readily justifies the use of Pd_{13} structures in this work. Moreover, since the diameters of the synthesized BNNTs were > 15 nm (Fig. 1), the curvature effect of the BNNTs on the interaction between Pd NPs and BNNTs was likely, not significant. Therefore, a BN sheet was used to model the BNNT structure, in which a $6 \times 6 \times 1$ supercell structure with a vacuum layer of 20 Å was used for the BN sheet. For comparison, a graphene structure was also used as a representation of the carbon support.

Free energy calculations were performed by employing the computational hydrogen electrode (CHE) model [43]. In this model, the chemical potential of $H^+ + e^-$ was considered to be equal to that of the gas-phase ½ H_2. The Gibbs free energy change for the H adsorption
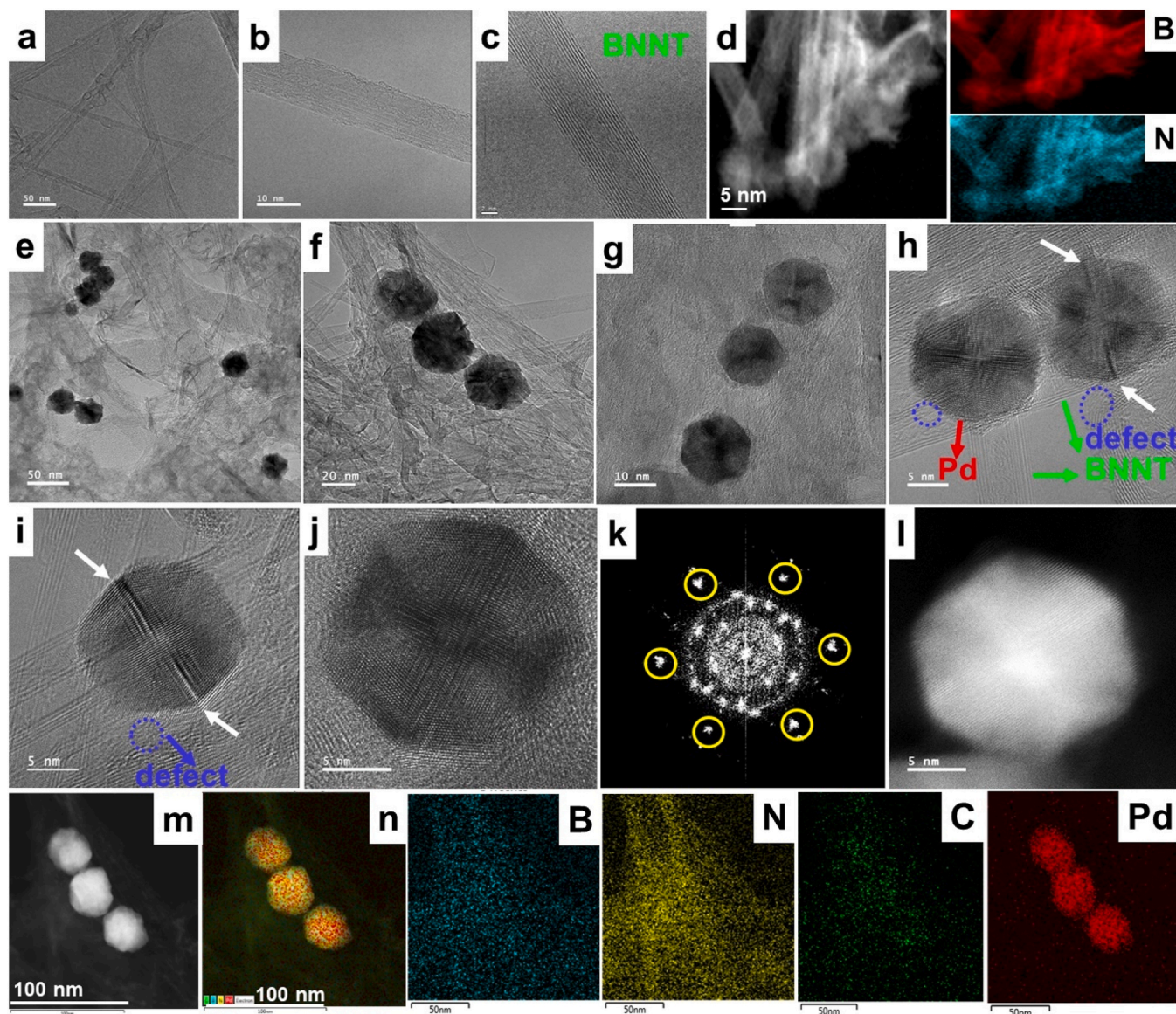

Fig. 1. a-d) TEM, HRTEM and, EELS mapping images of pristine BNNT, e-l) TEM, HRTEM, fast Fourier transform (FFT) and STEM images of IC-Pd@BNNT, m, n) HAADF-STEM, and elemental mapping images of IC-Pd@BNNT. White arrows indicate the presence of multi-twin boundaries. Scale bar (a-c) is 50 nm, 10 nm, 2 nm and (j) is 5 nm.

(ΔG_{H*}) was calculated as follows:

$$\Delta G_{H*} = \Delta E + \Delta ZPE - T\Delta S \tag{9}$$

where ΔE is reaction energy calculated by DFT, ΔZPE is the zero-point energy correction, and $T\Delta S$ is the entropic correction. The $\Delta ZPE - T\Delta S$ term is corrected according to Nørskov et al.,[44] $\Delta G_{H*} = \Delta E + 0.24$ eV.

To describe the stability of Pd NPs supported on BNNTs, the adsorption energies of Pd NP ($\Delta E_{ad\ Pd}$) on various BN sheet structures were calculated using the following equation:

$$\Delta E_{ad\ Pd} = \Delta E_{system} - \Delta E_{Pd} - \Delta E_{support} \tag{10}$$

where ΔE_{system} is the total system energy of Pd adsorbed on the support, ΔE_{Pd} is the total energy of the free Pd NP, and $\Delta E_{support}$ is the total energy of the support.

The charge density difference (CDD) was also determined to show how the charge densities of Pd NPs changes by BN and carbon supports. This was calculated by the following equation:

$$\Delta\rho = \rho_{AB} - \rho_A - \rho_B \tag{11}$$

where ρ_{AB}, ρ_A, and ρ_B are the charge densities of the total system, the Pd NP, and the support material, respectively.
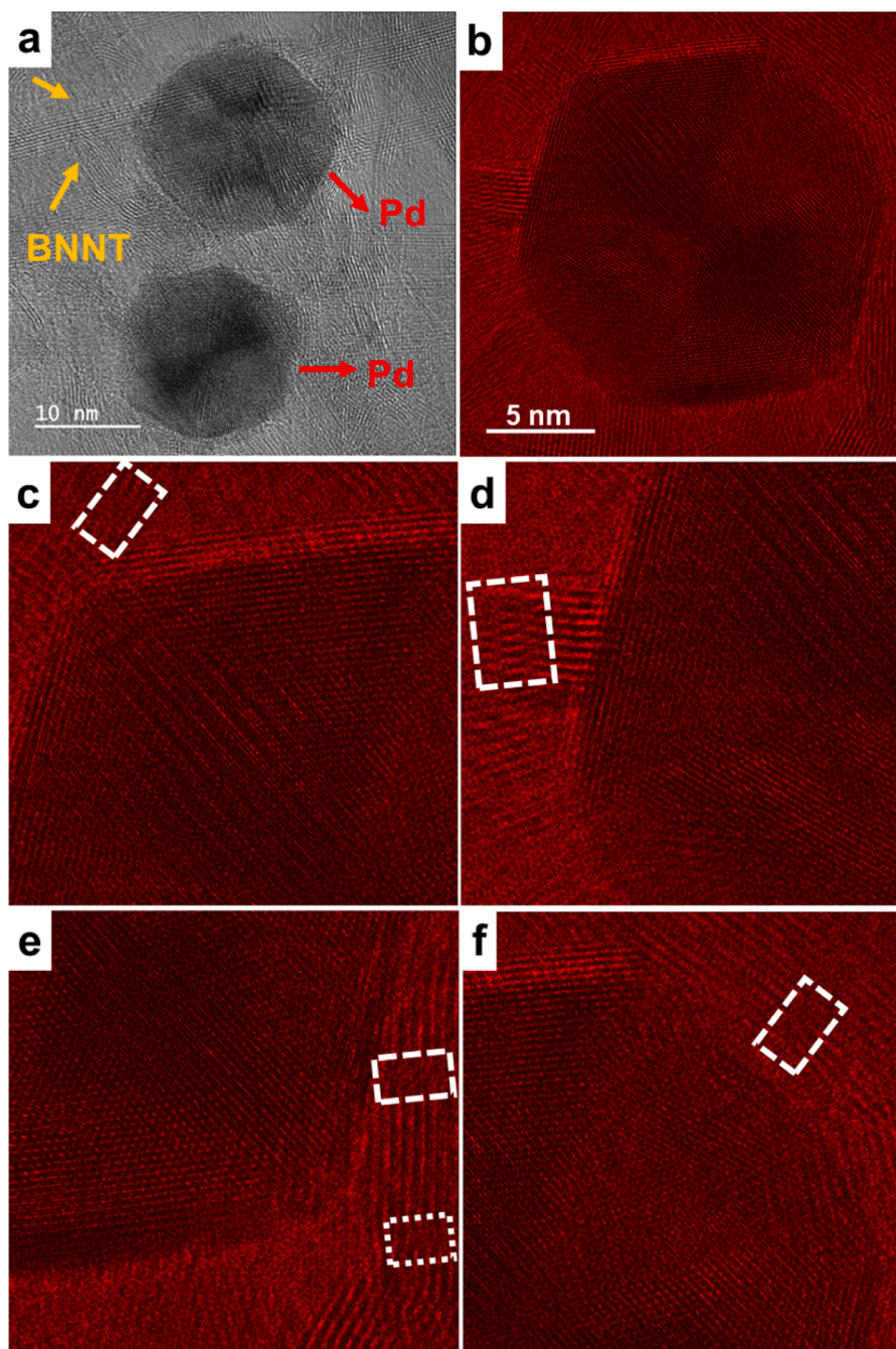

Fig. 2. a, b) HRTEM image of IC-Pd@BNNT and c-f) expended view images of (b). White squares indicate the defect sites of BNNT support.

3. Results and discussion

3.1. Structural and morphological characterization

BNNTs were purified, and the IC-Pd@BNNT catalysts were synthesized using a solvothermal method (Scheme 1) in the presence of N, N-dimethylformamide (DMF) which can act as a solvent, surfactant, and stabilizing agent to produce more catalytically active sites through an external surfactant-free strategy (see experimental section) [45].

The transmission electron microscopy (TEM) and high-resolution TEM (HRTEM) images showed that the purified BNNT was composed of a multi-walled structure that had defects (Fig. S1, S2), while the EELS mapping of this catalyst confirmed the presence of B and N moieties

(Fig. 1a-d). In addition, electron paramagnetic resonance spectra (EPR) can provide more evidence of the presence of defects states of BNNT. The purified BNNT displayed a symmetrical EPR signal with a g value of g= 2.008 as shown in (Fig. S3), which confirms the presence of defects in the BNNT structure. The icosahedral Pd NPs were widely distributed on the surface of BNNT.

The Pd NPs exhibited a uniform IC shape, with a size of approximately 20 to 30 nm, and a 2-fold axis of symmetry, as well as a 3-fold axis oriented parallel to the electron beam, indicating that the IC-Pd NPs on BNNT had multi-twin boundaries (white arrow) and defects (violet circles) (Fig. 1e-j). Additionally, the corresponding fast Fourier transform (FFT) spots (Fig. 1k) highlighted the hexagonal symmetry and high crystallinity of IC-Pd (111) plane [46]. The HAADF-STEM image
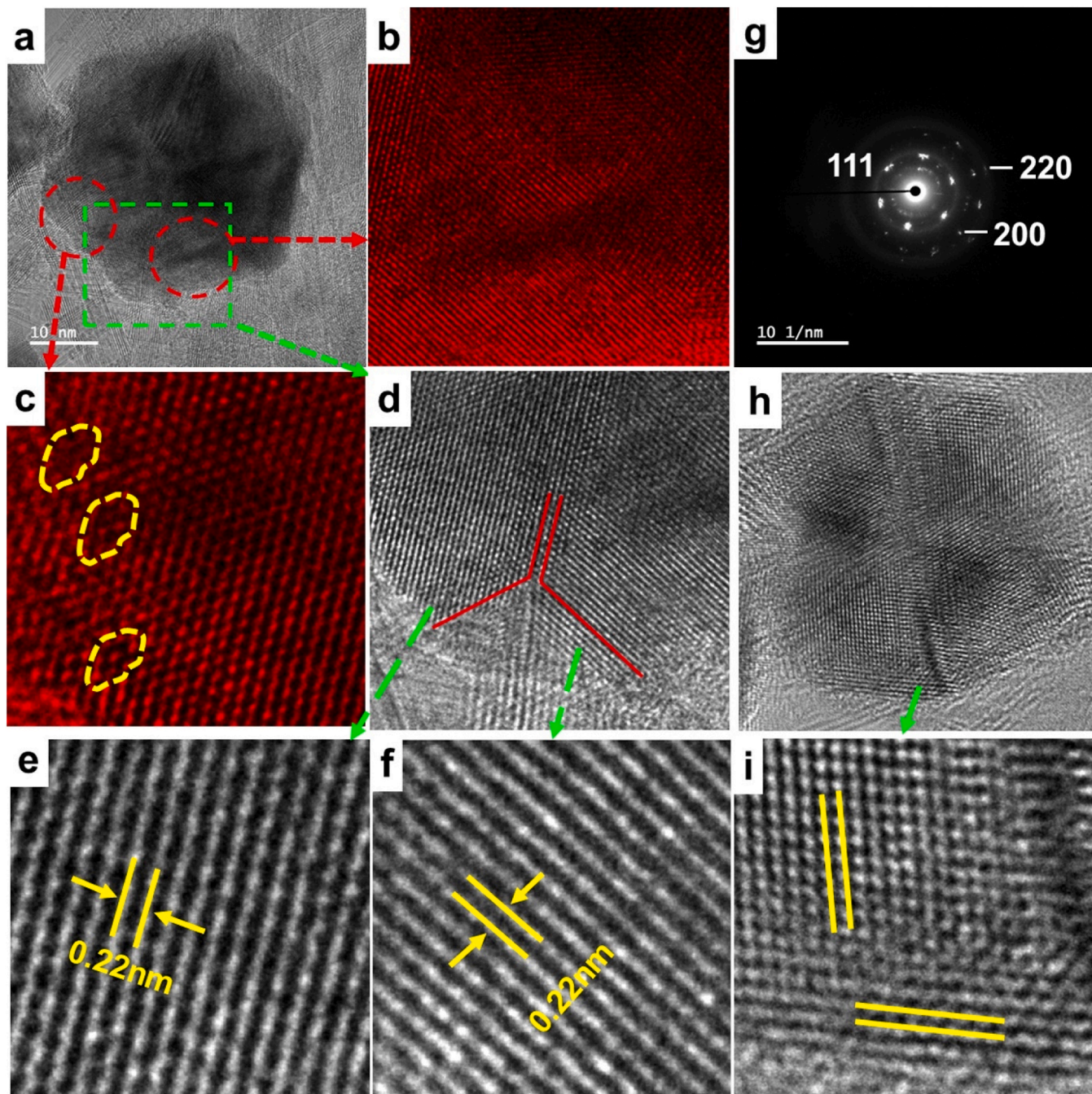

Fig. 3. a) HRTEM image of IC-Pd@BNNT and it expended view images (b-f), g) SAED pattern, h, i) HRTEM and it expended view image of IC-Pd@BNNT with twin boundary defects. The yellow circles, green arrow, red borders, and white mark indicate the twin boundaries and defects of the IC-Pd NPs on BNNT.

(Fig. 1i) confirmed that the Pd NPs on BNNT were IC shaped, and.

STEM elemental mapping corroborated this finding, indicating that the IC-Pd NPs are surrounded by B, N, and a small portion of C atoms on the BNNT surface (Fig. 1 m, n). Additionally, STEM images displayed line mapping, EDS of IC-Pd@BNNT (Fig. S4). Further, Fig. 2 illustrates the HRTEM images having the vacancy defects of BNNT in the IC-Pd@BNNT catalyst (white squares). In addition, the 3-fold axis of symmetry of IC-Pd, showing its face defects and twin boundaries (red circles and green square) (Fig. 3). The extended view of Fig. 3b, c highlights the presence of face defects (yellow), while Fig. 3d-f shows the twin boundaries, each with a lattice spacing of 0.22 nm, indexed to the (111) plane of Pd [47]. The SAED pattern shows the high crystalline nature of IC-Pd with the planes of (111), (200) and (220) (Fig. 3g). IC-Pd NPs encased in BNNT exhibited similar properties to a twin plan with face defects (Fig. 3h, i). The combination of (111) facets and twin boundaries on the IC-Pd surface enhanced the electrochemical activity of the catalyst [48]. An IC structure with 5, 3, and 2-fold axes of symmetry was observed by implementing a tomography tilt series using a dark-field scanning transmission electron microscopy (ADF-STEM). The 5-fold symmetry was expressed by the 42.5° and 40.5° tilt angles, while the tilt angles 12.5° and 10.5° showed the 3-fold axis of symmetry. The tilt angles of − 5.5° and − 7.5° represented the symmetry of the 2-fold axis, which was oriented parallel to the electron beam of IC-Pd@BNNT (Fig. 4). Whereas the total tilt of 61 STEM images were collected from 2D projections of a 3D object (as shown in (Fig. 4) pink), the corresponding 3D tomography video of IC-Pd@BNNT (Video S1) clearly showed tilting owing to the presence of the BNNT support. The tilting series of 2D projection images and the 3D tomographic video provided a complete structural view of IC-Pd on BNNT. Furthermore, the TEM, EDS, and STEM elemental mapping images of bare Pd NPs are shown in Fig. S5a, b (HR–TEM, FEI Technai at the Center for Bionano Materials Research at Gachon University). Interestingly, the absence of BNNT in the DMF medium resulted in the agglomeration of the Pd NPs, and no icosahedral shapes were formed (Fig. S5a). This indicates that BNNT acts as a template support for nucleation in the formation of IC-Pd, through the reaction between Pd and the N moiety, where the facet interaction matches with the B_3N_3 ring, and accelerates the growth of polyhedron clusters. In addition, the synthesized TEM, STEM elemental mapping images of IC-Pd@BNNT-L, and IC-Pd@BNNT-H are shown in Fig. S6 and S7. The IC-Pd@BNNT-L particles size appeared 15.5 nm uniformly distributed shown in Fig. S6 (a-d), whereas Fig. S7 (a-e) illustrates the TEM and HAADF-STEM elemental mapping of IC-Pd@BNNT-H and the particles size appeared ~35.5 nm and slightly agglomerated. The nucleation and growth mechanisms of Pd nanoclusters were theoretically explained by-Schimmenti et al. [49], which corresponds with the experimental results of this study. The above results were further explained by X-ray photoelectron spectroscopy (XPS), EXAFS, and Raman spectroscopy techniques. In addition, Pd NPs supported on 2D carbon–nitrogen (CN) moieties (Pd/CN) were synthesized for comparison. Fig. S8a, b illustrates the TEM, EDS, and elemental mapping images of Pd/CN that indicate the presence of icosahedral Pd embedded on the surface of 2D CN. The EDS and elemental mapping showed the presence of C, N, O, and Pd. The phase purity of the BNNT, bare Pd nanoparticles (NPs), IC-Pd@BNNT and Pd@CN was analyzed by Powder X-ray diffraction (PXRD) and Raman spectroscopy. The diffraction peaks located at 25.74º, 42.048º, and 53.08º corresponded to the crystalline planes (003), (101), and (006) of BNNT, respectively (Fig. 5a (i)). The major diffraction peak located at 40.1° represented the (111) plane of Pd NPs, while the peaks at 46.64° and 68.10º represented the (200) and (220) crystalline planes of Pd NPs (Fig. 5a (ii)), respectively. Similar diffraction peaks at 40.06°, 46.59°, and 68.99° were observed for the IC-Pd@BNNT catalysts (30 mg, 60 mg, 100 mg), but the (111), (200), (220) planes are marginally shifted to a lower 2-theta value (Fig. 5a (iii-v)). This shift was due to the nucleation and growth of IC-Pd NPs on the BNNT surface, whereas in addition, crystalline planes of Pd NPs Fig. 5a(vi) illustrates a new peak at 25.54º belongs to the (002)

plane of graphitic carbon nitride of Pd@CN catalyst. The chemical composition and environmental coordination of the IC-Pd@BNNT catalyst were elucidated by XPS, where peaks at 190 eV, 284 eV, 398 eV, and 532 eV corresponded to the B 1 s, C 1 s, N 1 s, and O 1 s, respectively (Fig. 5b (i)). Additionally, a peak at 337 eV represented the Pd 3d (Fig. 5b(ii)), showing the presence of B, C, N, O, and Pd elements in the pristine BNNT and IC-Pd@BNNT catalyst. The atomic percentages of the pristine BNNT and IC-Pd@BNNT catalysts are shown in Table S1, with the pristine BNNT having a combined atomic percentage of B and N higher than 91%, while the remaining percentages of C and O were 4.36% and 3.18%, respectively. The low proportion of C and O in pristine BNNT was possibly owing to the washing with methanol. Similarly, the IC-Pd@BNNT catalyst had a combined atomic percentage of B and N of approximately 70%, while the percentages of C and Pd were approximately 21% and 1.28%, respectively. The proportion of C in the IC-Pd@BNNT catalyst was owing to the use of DMF as a solvent during synthesis, and its presence was confirmed by the STEM elemental mapping image (Fig. 1 n) [50]. This C moiety triggered the conductivity of the BNNT. The deconvolution spectra (Fig. 5c,d) of B 1 s and N 1 s showed peaks at 190.9 eV and 398.3 eV for pristine BNNT (i) and at 191.1 eV and 398.6 eV for the IC-Pd@BNNT catalyst (ii), highlighting the interaction between the B_3N_3 ring and the facet of IC-Pd, particularly that of the coordination interaction between the IC-Pd NPs and the N moieties [30]. The deconvolution spectra of C 1 s and O 1 s of the IC-Pd@BNNT catalyst are shown in Fig. S9. In the deconvolution Pd 3d spectra, major binding energy peaks were observed at 335.38 eV and 340.78 eV representing the Pd^0 metallic state, while a shakeup peak at 337.78 eV indicated the presence of Pd^{2+}. The XPS data of IC-Pd@BNNT-L, IC-Pd@BNNT-H, and Pd@CN is shown in Fig. S10, S11. To develop a further understanding of the oxidation and coordination environment of the IC-Pd@BNNT catalyst, synchrotron-based X-ray absorption near edge structure (XANES) and extended X-ray absorption fine structure (EXAFS) experiments were performed. The Pd K edge XANES of IC-Pd@BNNT catalyst was similar to that of Pd foil, indicating that the IC-Pd was in the metallic state, (Fig. 5 f). Further, the Fourier-transform Pd K-edge EXAFS showed the local coordination between IC-Pd NPs and BNNT, with the peaks at 1.54 Å and 2.5 Å indicating the presence of Pd-N and Pd-Pd metallic sites (Fig. 5 g). The above results were consistent with the XPS data, supporting the finding that the coordination of IC-Pd@BNNT was Pd-N. This coordination environment is further clarified by DFT calculations in Section 3.3. Tauc's plot was used to determine the optical band gap of the developed IC-Pd@BNNT and bare BNNT [24–26]. The plot showed a bandgap of 3.7 eV for the IC-Pd@BNNT catalyst (Fig. 5 h (red line)) and 4.93 eV for bare BNNT, which indicates that the chelation of IC-Pd on BNNT as well as C moiety decrease the band gap of developed IC-Pd@BNNT catalyst. The presence of C moiety in the interstices of the IC-Pd@BNNT catalyst enhanced the conductivity of the BNNT support. Specific surface area is a critical criterion for good electrochemical support materials. The pristine BNNT displayed a specific surface area of 230.57 m^2 g^{-1} with pore sizes of 11.25 nm and 31.71 nm, demonstrating its highly mesoporous character. However, IC-Pd@BNNT catalyst exhibited a specific surface area of 128.64 m^2 g^{-1} and a pore size of 3.76 nm, showing that the catalyst had excellent mesoporous character (Fig. 5i, Fig. S12a). The lower surface area of the IC-Pd@BNNT catalyst compared to the pristine BNNT was owing to the encasing of IC-Pd NPs. The mesoporous nature of BNNT and its defect sites initiate ion mobility and enhance the conductivity of the developed catalyst. The BET surface area and pore volumes of IC-Pd@BNNT-L, IC-Pd@BNNT-H catalysts, Pd@CN catalyst, and the pristine Pd NPs are shown in Fig. S12b-e and Table S2. The Raman peak for BNNT was observed at 1365 cm^{-1} as the characterization peak of pristine BNNT (Fig. 6(a) [51], whereas a peak at 1351 cm^{-1} represented a blue shift in the IC-Pd@BNNT catalyst (Fig. 6(b)), which was attributed to the interaction between the hexagon B_3N_3 ring and the IC-Pd NPs, interestingly the peak shifts was clearly visualized in 3D Raman spectra images. The chemical bonding of pristine BNNT and
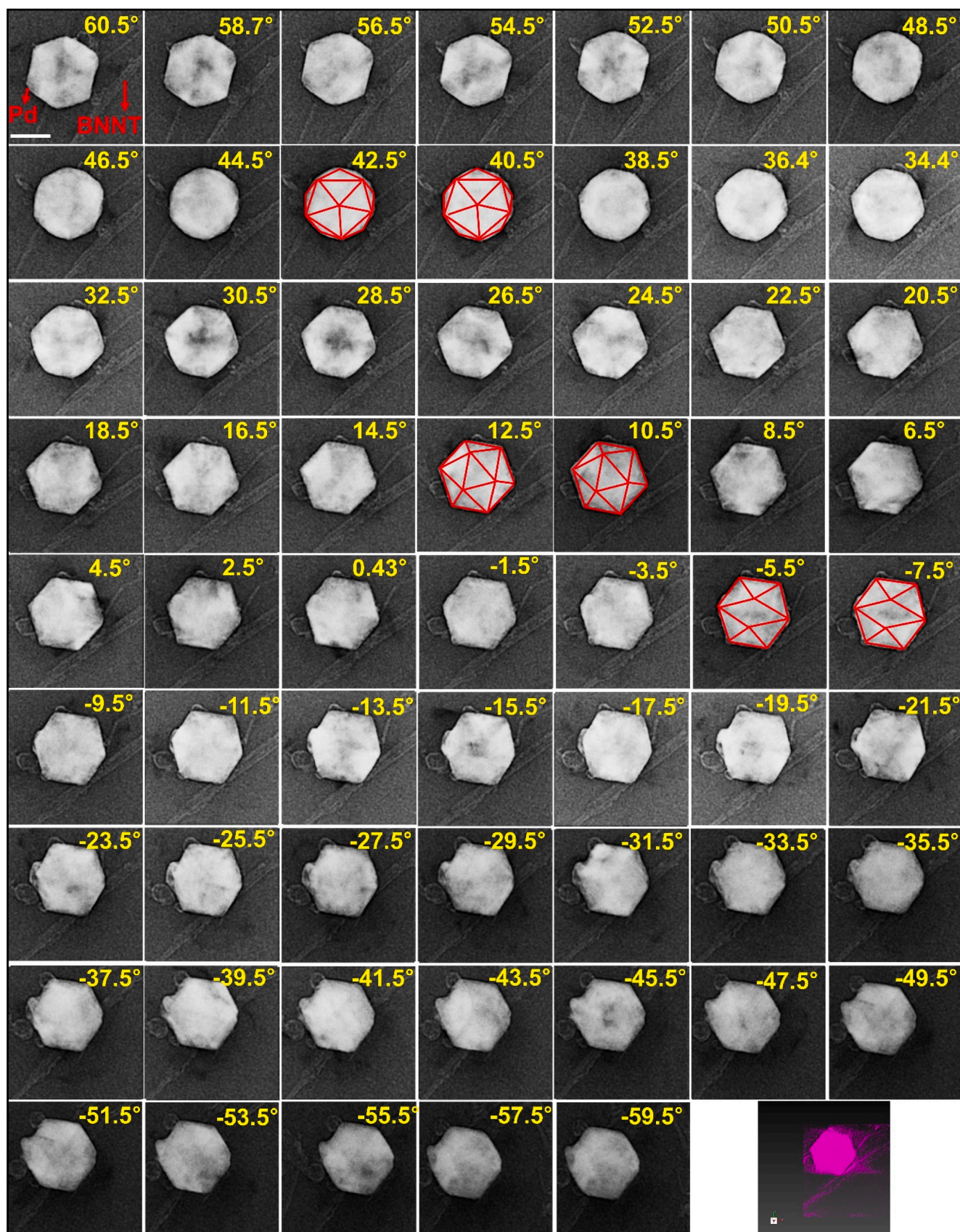
Fig. 4. HAADF-STEM images of IC-Pd encased BNNT by tilting series of 61 icosahedral 2D projection images from 3D tomographic tilt angles of + 60.5° to − 59.5°. Scale bar, 20 nm.
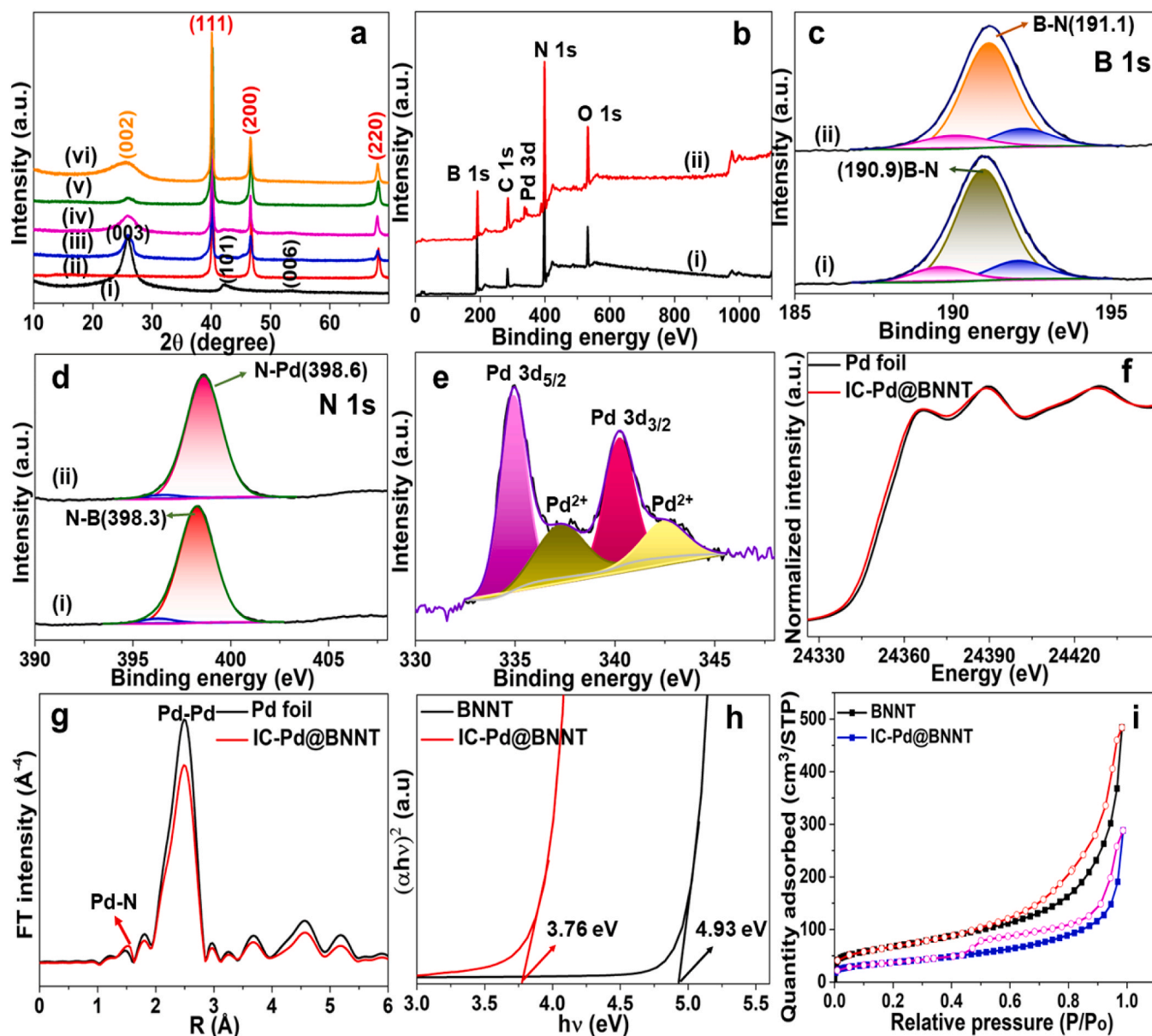
Fig. 5. a) (i-vi) PXRD of pristine BNNT, bare Pd NPs, IC-Pd@BNNT catalysts (30 mg, 60 mg, 100 mg), and Pd@CN respectively, b) XPS survey scan spectra of (i) pristine BNNT, (ii) IC-Pd@BNNT, c, d) deconvolution spectra of B 1 s and N 1 s of (i) pristine BNNT, and (ii) IC-Pd@BNNT, e) deconvolution spectra of Pd 3d of IC-Pd@BNNT, (f, g) XANES and EXAFS spectra of IC-Pd@BNNT and Pd foil, h) UV-Visible absorption spectra of the band gap calculation spectra, i) BET isotherms of pristine BNNT (black) and IC-Pd@BNNT (blue).

IC-Pd@BNNT was further studied using FTIR spectroscopy (Fig. S13i, ii). The peaks at 1343 cm^{-1} and 798 cm^{-1} showed the stretching and bending vibrations of B-N bonds; however, after BNNT was encased by IC-Pd, the peaks shifted to from 1343 cm^{-1}, 798 cm^{-1} to 1306 cm^{-1}, 766 cm^{-1}, highlighting the covalent interaction between IC-Pd and BNNT. The overall characterizations corroborate the existence of chemical coordination bonding and interactions within the IC-Pd@BNNT catalyst. Pristine BNNT is the most thermally stable material; therefore, the IC-Pd@BNNT should exhibit outstanding thermal stability. As shown in Fig. S14(i-v), the IC-Pd@BNNT was more stable than the other catalysts as there was less than 2% weight loss compared to that of C-supported Pd/CN (91%) and commercial (Pd/C-90%).

3.2. Electrochemical hydrogen evolution reaction

The electrochemical HER performance of the developed catalyst was evaluated using a three-electrode cell system with IR correction applied

to all polarization curves. Fig. S15 shows the IR correction applied polarization curves of various concentrations of IC-Pd@BNNT catalysts, and the overpotentials are shown in Table S3. At lower Pd concentration the number of electrochemical active sites (IC-Pd) are limited, whereas at higher Pd loading concentration the stacking nature of the catalyst results in an increase in the distance between the transport of electrons on the surface of the electrode and it would be too dense to allow efficient mass transport [52]. Therefore, the IC-Pd@BNNT (18.3 wt%) is selected as optimized catalyst throughout the study, compared to IC-Pd@BNNT (11.5 wt%) and IC-Pd@BNNT (29.4 wt%) catalysts. In Fig. 7a, the blank carbon paper electrode (CPE) substrate was not active for the HER (black line), while the pristine BNNT, bare Pd NPs, IC-Pd@BNNT, Pd@CN, Pd/C (30%), and Pt/C (20%) showed overpotentials of 381.1 mV, 68.3 mV, 5.7 mV, 101.6 mV, 47.4 mV, and 24.1 mV at a current density of − 10 mA cm^{-2}, respectively, and overpotentials of 418.6 mV, 83.8 mV, 15.7 mV, 127.4 mV, 62.6 mV, 29.4 eV at a current density of − 20 mA cm^{-2}, respectively (Fig. 7a). The
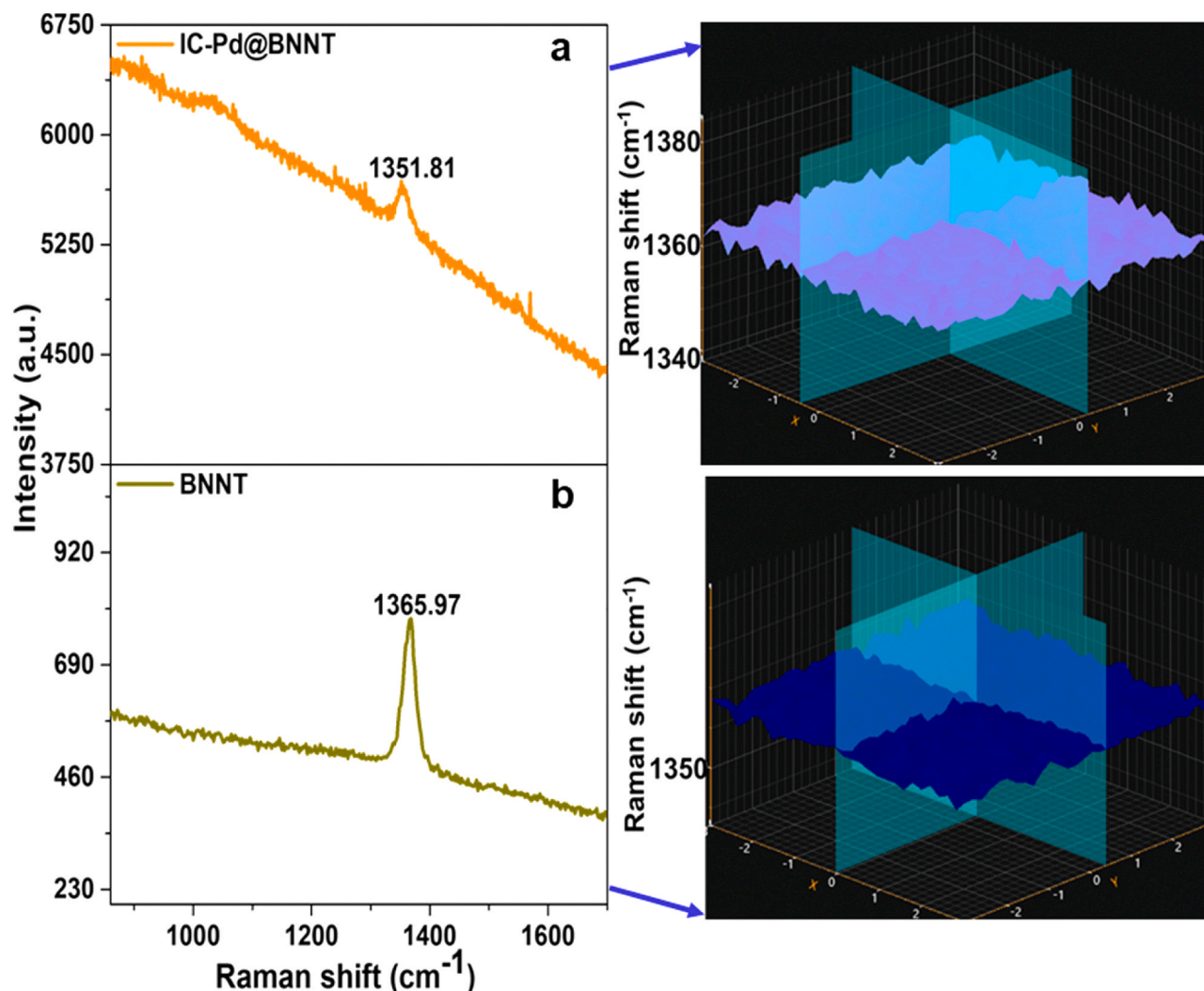
Fig. 6. a, b) Raman spectra and its 3D optical images of pristine BNNT and IC-Pd@BNNT.

IC-Pd@BNNT catalyst exhibited a lower overpotential than the pristine BNNT, bare Pd NPs, Pd@CN, Pd/C (30%), and even Pt/C (20%) catalysts at a current density of -20 mA cm^{-2}. However, at higher current densities of -100, -500, and -1000 mA cm^{-2}, the HER activity of the IC-Pd@BNNT catalyst competes with that of the commercial Pt/C (20%) and is approximately four times higher than that of Pd/C (30%). In addition, the contact angle (Fig. 7i and Fig. S16 a, b) illustrates that the developed IC-Pd@BNNT has hydrophobic surface (101.83°), due to the hydrophobic nature of the electrode the bubble ejection occurs forcefully and the LSV appeared roughly at higher current density (Fig. S15). Table S4 summarizes the overpotentials at various current densities and the Tafel slope values for the IC-Pd@BNNT electrode during the HER. The low overpotential and high current density for the IC-Pd@BNNT composite result from the defect sites of BNNT that may initiate the ion mobility and enhance the catalytic activity. The vacant defects of IC-Pd@BNNT have already been visualized (Figs. 2,3 and Fig. S1, S2), and the effect of vacancy defects on the HER catalytic activity will be further discussed theoretically in Section 3.3. The superior HER activity of the IC-Pd@BNNT catalyst as well as the quantity of catalyst loading were compared to those of previously reported Pd and Pt-based HER catalysts (Table S5). The low quantities of the C moiety present in IC-Pd@BNNT decreased the energy barrier and accelerated the reaction kinetics. The Tafel slope of IC-Pd@BNNT was 35.7 mV dec^{-1} (Fig. 7b), indicating accelerated kinetics during the HER. The rate-determining step followed the Volmer–Heyrovsky reaction path [53]. The

overpotentials of the developed IC-Pd@BNNT catalyst, Pd/C (30%), and Pt/C (20%) were compared at various current densities (Fig. 7c). The CV of IC-Pd@BNNT at various scan rates from 20 to 100 mV s^{-1} under the non-Faradaic current region (0.00 to -0.1 V (vs. AgCl)) was performed (Fig. 7d), and the corresponding double layer capacitance (Cdl) was 0.55 mF cm^{-2} (Fig. 7e). The ECSA and BET normalized overpotential showed that the defect site of IC-Pd@BNNT (Fig. S17) had higher HER activity than pristine BNNT, bare Pd NPs, Pd@CN, commercial Pd/C (30%), and competed with Pt/C (20%) under 0.5 M H$_2$SO$_4$. Owing to the optimized electronic structure the enhanced HER activity of the IC-Pd@BNNT catalyst not only depends on increased ECSA but also follows the intrinsic activity. Further, The CV of bare Pd NPs, Pd@CN catalyst at various scan rates from 20 to 100 mV s^{-1} under the non-Faradaic current region (0.00 to -0.1 V (vs. AgCl)) was also performed (Fig. S18 a, b), and the corresponding double layer capacitance (Cdl) was 0.207 mF cm^{-2} and 0.35 mF cm^{-2}. The calculated values of the mass activity, specific activity, ECSA, roughness factor (RF), and turnover frequency (TOF) are summarized in Table S5 S6. The IC-Pd@BNNT catalyst exhibited high mass activity (620.31 A g$_{Pd}^{-1}$) compared to bare Pd NPs, Pd@CN catalyst and good specific activity (45.11 mA cm$_{ECSA}^{-2}$).

Electrochemical impedance spectroscopy (EIS) was used to study the electron transfer rate reaction of the synthesized catalyst materials. Electrochemical impedance spectroscopy (EIS) was used to study the electron transfer rate reaction of the synthesized catalyst materials frequencies ranging from 100 kHz to 0.1 Hz at the open circuit potential
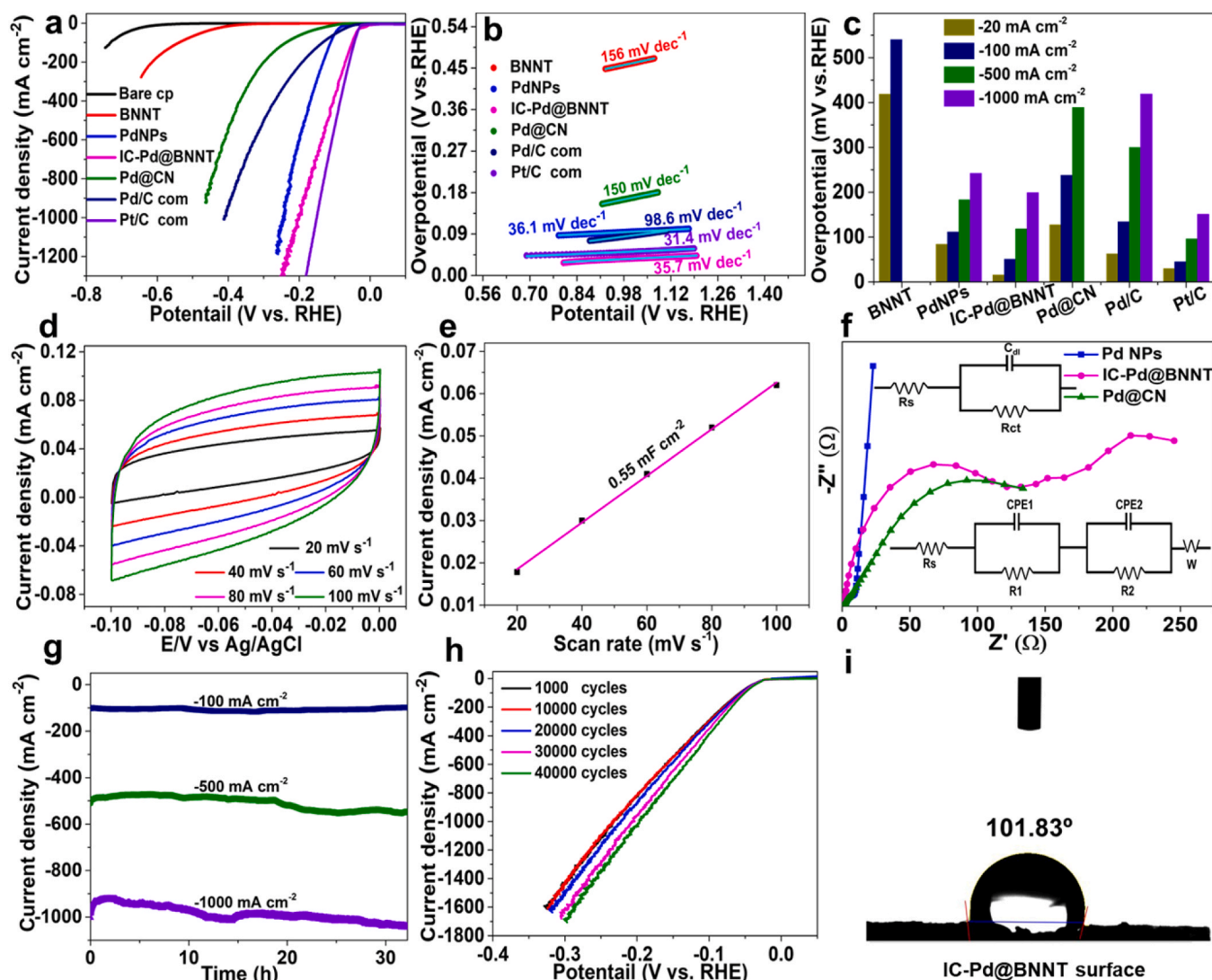
Fig. 7. a) IR corrected polarization curves of CP, BNNT, Pd NPs, IC-Pd@BNNT, Pd@CN, Pd/C (30%) and Pt/C (20%) at the scan rate of 2 mV s^{-1} in 0.5 M H$_2$SO$_4$, b) the Tafel plot extrapolated from the LSV studies, c) a bar graph of overpotentials at various current densities, d-e) Cyclic voltammetry at different scan rates and double layer capacitances (Cdl) of IC-Pd@BNNT catalysts, f) Nyquist plots (EIS) of the as-synthesized pristine BNNT, Pd NPs, IC-Pd@BNNT, and Pd@CN, g) long-term durability test by chronoamperometry in 0.5 M H$_2$SO$_4$ at various current densities, h) Polarization curves recorded from 1000 to 40000 CV cycles in 0.5 M H$_2$SO$_4$ at a scan rate of 2 mV s^{-1}, i) digital image of measurement of contact angle IC-Pd@BNNT surfaces.

with an amplitude of 10 mV. The charge transfer resistance (Rct) of bare Pd NPs (4.2 Ω), IC-Pd encased in BNNT (133.5 Ω) was significantly lower than that of pristine BNNT (2791 Ω-See SI Fig. S19), suggesting that the IC-Pd@BNNT catalyst had higher conductivity than pristine BNNT (Fig. 7f). The lower charge resistance of IC-Pd@BNNT was attributed to the symbiotic electron transfer between IC-Pd and the C content of BNNT. Furthermore, from the EIS the equivalent circuit fitting model of IC-Pd@BNNT (Fig. 7f lower inset) reveals the R$_s$, R$_1$, R$_2$, CPE and W represent the solution resistance, electrode porosity, charge transfer resistance, respectively. Constant phase angle element (CPE) indicates the double layer capacitance of the electrode, and W is the Warburg element. Fig. 7f upper inset shows the equivalent circuit fitting of bare Pd nanoparticles.

In practical applications, the durability of catalysts plays a crucial role. In electrocatalysis, catalysts generally are susceptible to low stability because of the leaching of electrode materials into the solution. The long-term stability of the developed IC-Pd@BNNT catalyst was evaluated using chronopotentiometry by continuous monitoring for 32 h in a 0.5 M H$_2$SO$_4$ solution (Fig. 7g) at current densities of − 100 mA cm^{-2}, − 500 mA cm^{-2}, and − 1000 mA cm^{-2} respectively.

The hydrogen evolution at higher current density (−1000 mA cm^{-2}) shown in video S2, reveals that bubble (H$_2$) ejection enormously increases at higher current density. The IC-Pd@BNNT catalysts exhibited high stability even at higher current densities and overpotentials. In addition, the durability of the IC-Pd@BNNT was investigated over 40000 CV cycles in 0.5 M H$_2$SO$_4$ at scan rate of 100 mV s^{-1} within the potential range of − 1 to 0 V (vs. RHE), as shown in Fig. 7h. The assessment of the durability of the IC-Pd@BNNT catalyst showed exhibited zero loss reduction potential, highlighting the outstanding activity and stability of the developed BNNT-supported catalyst (Fig. 7h). Moreover, the catalyst was stored in 0.5 M H$_2$SO$_4$ solution for 304 days to investigate its structural and morphological integrity over the long term. The TEM, HRTEM, FFT, and EDS images taken after the 304-day period showed no IC-Pd structural damage, and the highly crystalline nature remained intact (Fig. S20). The aforementioned results suggest that the developed IC-Pd@BNNT catalyst has outstanding durability. Fig. 8a illustrates the electrochemical H-cell, in which the working and counter (Pt) electrodes were separated by a Nafion 117 membrane. The Faradaic efficiency (FE) of the IC-Pd@BNNT catalyst for hydrogen evolution in a 0.5 M H$_2$SO$_4$ electrolyte was assessed across
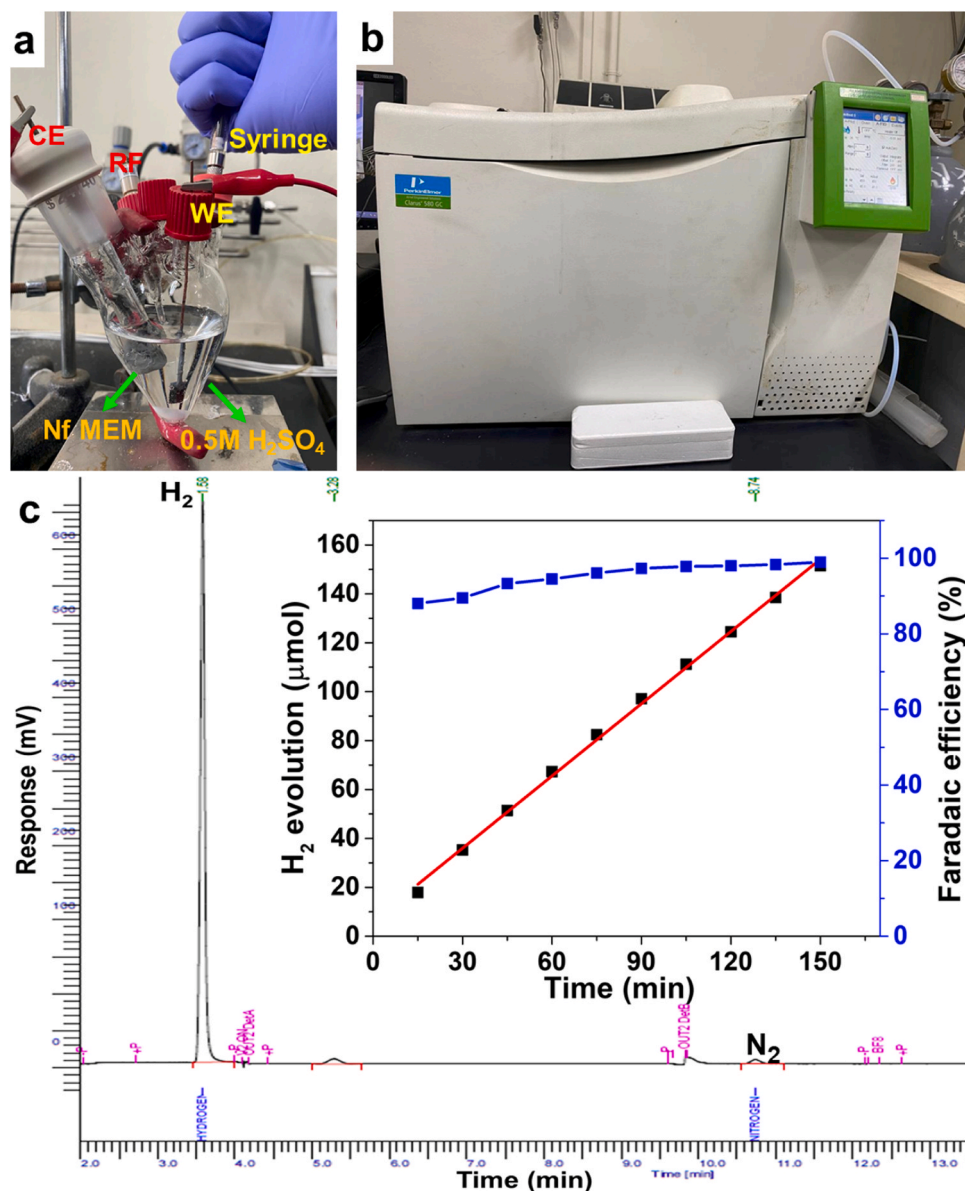
Fig. 8. a) digital image of Electrochemical H-cell, the working and counter (Pt) electrodes were separated by a Nafion 117 (Nf) membrane, b) digital image of gas chromatography (GC) equipment setup, c) H_2 gas quantification chromatogram image acquired at 150 min; inset shows the graph of the Faradaic efficiency and no of mole of H_2 gas obtained with time.

various time intervals, and the produced H_2 gas was evaluated by gas chromatography Fig. 8b. The FE was achieved 98.96% as shown in Fig. 8c. In addition, the chromatograms with various time intervals were shown in Fig. S21-29.

After long-term stability and durability test, the structural morphology and chemical composition of IC-Pd@BNNT were examined by TEM, HRTEM, EDS, and HAADF-STEM elemental mapping, as shown in Fig. S30-33. The STEM mapping supported the finding that the shape of the IC-Pd NPs in the IC-Pd@BNNT catalyst partially changed, and the sulfur moiety was present on the surface of IC-Pd, indicating that IC-Pd encased on BNNT acted as an excellent active phase. The chemical composition and electronic structure of the post-IC-Pd@BNNT catalyst were observed by XPS and PXRD spectrometry. The post-IC-Pd@BNNT wide scan XPS spectra showed that the peaks at 190 eV, 284 eV, 337 eV, 398 eV, and 532 eV were attributed to B 1 s, C 1 s, N 1 s, O 1 s, and Pd 3d, respectively. A new peak at 168 eV was attributed to S 2p (Fig. S34), indicating the presence of S 2p along with B, C, N, O, and Pd (Fig. S35, Table S7). The crystallization and phase purity of post-IC-

Pd@BNNT did not change, as shown by the PXRD data (Fig. S36 (i, ii)). The aforementioned post-microscopic and spectroscopic techniques suggest that the developed IC-Pd@BNNT has outstanding durability. However, the microscopic and spectroscopic techniques may not fully explain the IC-Pd@BNNT active phase site. Therefore, theoretical insights were used to elucidate the origin of the enhanced catalytic performance on the IC-Pd@BNNT at a molecular level. The details regarding the active site of the catalyst are explored in the following DFT section.

3.3. Computational analysis

DFT calculations were performed to understand the enhanced HER catalytic activity of the IC-Pd NPs supported on BNNTs. The free energy change of H* (ΔG_{H*}, * denotes a surface site) is a well-known descriptor for the HER activity [44], wherein the higher HER catalytic activity occurs when ΔG_{H*} is closer to zero. Based on experimental results, four BN models were considered: pristine BN, defective BN with vacancies,

C-doped BN, and defective C-doped BN with vacancies.

The DFT calculations show that ΔG_{H*} on the free IC-Pd$_{13}$ NP is −0.40 eV for the facet site and −0.35 eV for the edge site. Since the H adsorption was not favorable for the vertex site, the H atom moves to the edge or facet sites (Fig. S38a). These results indicate that hydrogen preferentially adsorbs on the facet site. Considering the icosahedral Pd$_{55}$ NP (Fig. S38b), it is shown that as the size of Pd NPs increases, ΔG_{H*} increases, despite the preference of the H adsorption still on the facet site. For example, ΔG_{H*} on the facet site of the Pd$_{55}$ NP is −0.31 eV, which is higher than that of the facet site of the Pd$_{13}$ NP. For comparison, the H adsorption on the surface of Pd(111) has a ΔG_{H*} value of −0.28 eV (Fig. S39), which is higher (less negative) than that of the Pd$_{13}$ or Pd$_{55}$ NPs. Nonetheless, the adsorption energies on Pd NPs are stronger than those on the Pt(111) (−0.20 eV), irrespective of the size of Pd NPs. This implies that it is difficult for the free Pd NPs to achieve the higher HER activity than Pt catalysts, supporting the experimental results of this study (Fig. 7a).

On the B/N or C supports, the ΔG_{H*} values of Pd$_{13}$/BN (−0.36 eV) and Pd$_{13}$/C (−0.37 eV) are positively higher than that of the free Pd$_{13}$

NPs (Fig. 9a, Table S8). This indicates that the H adsorption on Pd NPs can be weaker on the C or BN support than on the free Pd$_{13}$ NPs owing to electron transfer from Pd to the BN or C support (Fig. 9b,c). The electron transfer leads to a downshift of the D-band center of Pd relative to the Fermi level, which weakens the adsorption of an intermediate on metal surfaces [54,55]. This behavior is more pronounced on the BN support than on the C support (Fig. 9d, e). As observed in our experiment (Fig. 5 g), the interaction between Pd NPs and BN sheets occurs mainly through Pd-N bonds (Fig. 9c). And more electrons can be transferred in Pd-N bonds than Pd-C bonds due to the higher electronegativity of N in comparison to C. Therefore, the H adsorption on the Pd$_{13}$/BN is weaker than that of the Pd$_{13}$/C or free Pd$_{13}$ NPs. Although the BN support has a positive effect on HER catalytic activity, it is still unclear why the icosahedral Pd NPs supported on BN show a comparable HER activity to Pt/C in this study, as Pd13/BN has a much lower ΔG_{H*} than that of Pt (111).

Further DFT calculations reveal that B/N vacancies observed in our experiments (Figs. 2–3, S1-S3) are the main factors that can enhance the HER activity on the IC-Pd@BNNT catalyst. As shown in Fig. 9a and
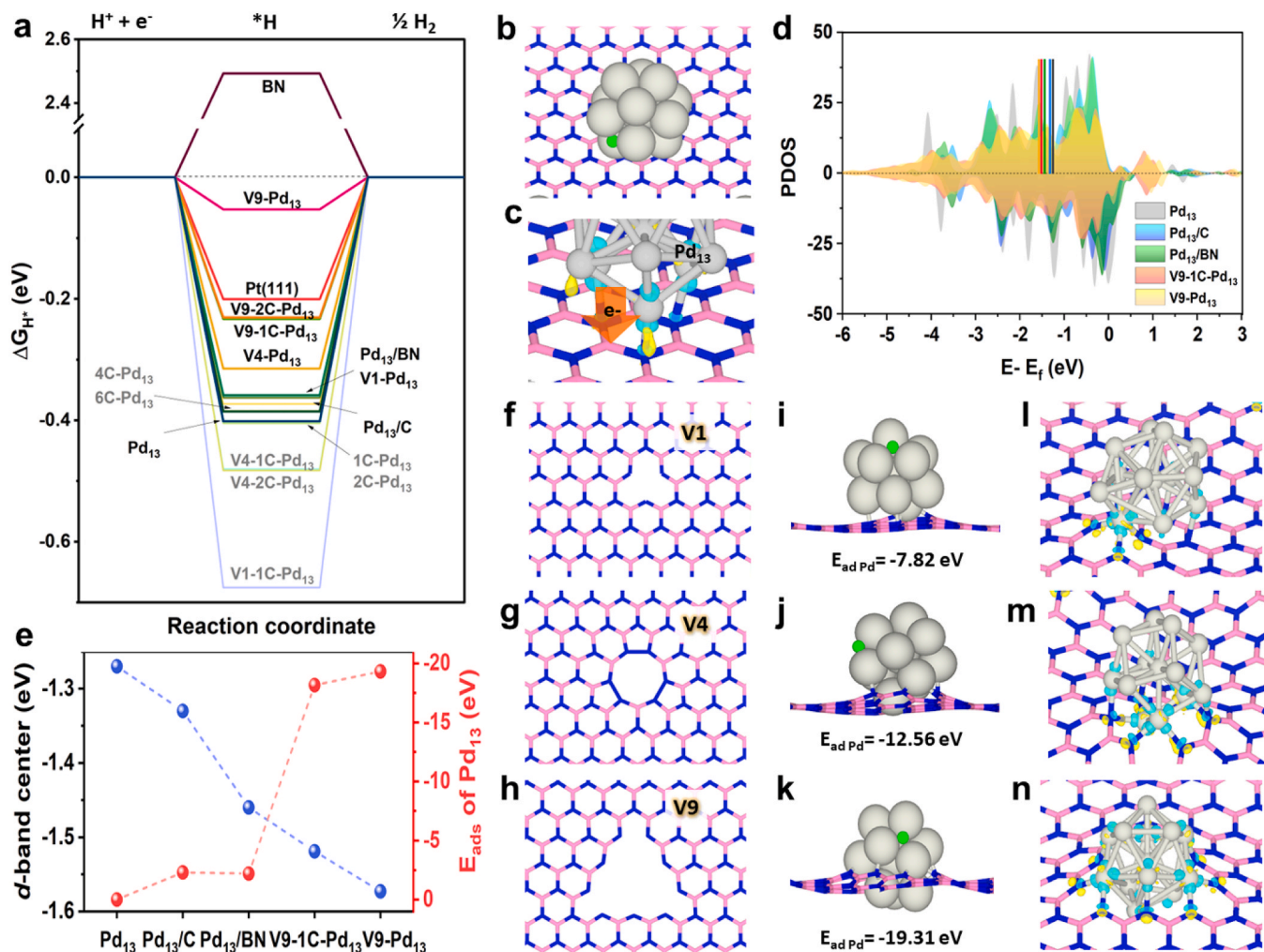

Fig. 9. DFT calculation results. (a) Free energy diagram at equilibrium potential (U = 0 V) for the HER activity on the Pd$_{13}$ NP supported on various BN supports. For comparison, Pd$_{13}$ on a carbon (graphene) support, pristine BN nanosheet (BN), and Pt(111) are considered. (b) The H adsorption geometry and (c) CDD of Pd$_{13}$ on a pristine BN nanosheet. The yellow and cyan isosurface (± 0.008 e/Bohr³) indicate accumulation and depletion of the charge density, respectively. (d) Projected density of states (PDOS) for the Pd d-orbitals of Pd$_{13}$, Pd$_{13}$/C, Pd$_{13}$/BN, V9–1 C-Pd$_{13}$, and V9-Pd$_{13}$. The D-band centers are shown using vertical lines (Pd$_{13}$ - gray, Pd$_{13}$/C - blue, Pd$_{13}$/BN – green, V9–1 C-Pd$_{13}$ – red, and V9-Pd$_{13}$ – yellow). (e) Changes of D-band centers and Pd$_{13}$ adsorption energies on various types of supports. (f-h) The optimized geometries for three types of defective BN supports: (f) V1 for 1-site vacancy, (g) V4 for 4-site vacancy, and (h) V9 for 9-site vacancy. (i-k) H adsorption geometries on Pd$_{13}$ supported on three different defective BN nanosheet: (i) V1-Pd$_{13}$, (j)_V4-Pd$_{13}$, and (k) V9-Pd$_{13}$. The binding energies of Pd$_{13}$ with the defective BN sheet (E$_{ad\ Pd}$) are included. (l-n) CDDs (isosurface ± 0.02 e/Bohr³) of Pd$_{13}$ adsorbed on the (l) V1, (m) V4, and (n) V9 BN nanosheet. Here, color codes for the atoms are B = pink, N = blue, Pd = gray, and H = lime green.

Table S8, ΔG_{H*} of Pd_{13} supported on defective BN sheets with B/N vacancies increases as the vacancy size increases. Interestingly, when Pd_{13} NP is supported on the BN sheet with a vacancy of nine B/N atoms (V9-Pd_{13}), the HER activity is superior to that of the Pt catalyst. This shows that vacancies in the BN support can significantly enhance the HER activity of Pd/BNNT catalysts. In Fig. S41, when Pd_{13} NPs are supported on C-doped BN sheets, the ΔG_{H*} values marginally change depending on the number of carbon dopants for 1 C to 6 C atoms (~ -0.40 eV). These values are much lower than that on the pristine BN support. Including B/N vacancies on the C-doped BN supports improves the HER activity of Pd_{13} NPs compared to that of non-defective C-doped BN supports (Fig. S42). For example, ΔG_{H*} is -0.40 eV on Pd_{13}/1 C-doped BN with no vacancies: however, the value increases to -0.23 eV on Pd_{13}/1 or 2 C-doped BN with a 9-site vacancy, which is comparable to that on the Pt(111). Based on these results, it is concluded that the superior HER activity of IC-Pd/BNNT (Fig. 7a) mainly results from the vacancies found in the BNNT supports. Although the C doping on BNNT supports does not chemically affect the HER, it can enhance the electrical conductivity of the BNNTs, leading to the enhanced electrochemical catalytic reactions.

The vacancies on the BNNT readily enhance not only the HER activity but also the stability of the catalyst. This results from the strong anchoring of the IC-Pd NPs onto the BN surfaces in the presence of vacancies. When Pd_{13} NPs bind to the pristine BN sheet, the binding energy is -2.3 eV. However, it significantly decreases on the defective BN sheet (e.g., -19.31 eV for V9-Pd_{13} in Fig. 9k) as the Pd binding energy increases when the size of the vacancy defect increases. The bigger vacancy size allows for the formation of more Pd-N bonds, strengthening the interaction between the Pd NP and BN support. As a result, the stronger interaction between the Pd NP and BN support leads to the transfer of more electrons from Pd to BN and makes H adsorption weaker (Fig. 9l-n). For this reason, the synthesized IC-Pd@BNNT catalysts exhibit excellent stability during the HER experiments (Fig. 7g-h).

In order to confirm that the active sites for the HER are surfaces of the Pd NPs, we further investigated the HER activity of BN surfaces by calculating ΔG_{H*} on the BN surface without Pd NPs. The H adsorption on pristine BN is unfavorable ($\Delta G_{H*} = 2.49$ eV, Fig. 9a), indicating that the pristine BN surface hardly contributes to the HER activity. With respect to the C-doped BN surfaces (Fig. S43, S44), ΔG_{H*} is ranged between 1.29 and 2.48 eV depending on the number of C dopants. A graphene surface, for comparison, has a ΔG_{H*} of 1.66 eV. Although the ΔG_{H*} values of the C-doped BN surfaces are lower than that of the pristine BN surfaces, the HER activity on the C-doped BN surfaces is still very low compared to that on the Pt(111) surface. These results were similar to those of previous studies [56,57]. On the C-doped BN surfaces with vacancies (Fig. S45), H adsorption is much stronger owing to the bond formation with the dangling N atom. As the vacancy size increases, the H adsorption becomes even stronger. From these DFT calculations, it is confirmed that the BN surfaces do not play a role in the active site for HER activity even though they are doped with carbon atoms or have B/N vacancies. Therefore, it is concluded that the main active sites of IC-Pd NPs supported on BNNT for HER activity are the Pd surfaces.

4. Conclusions

Designing unique catalytic supports for the active metallic site other than carbon is an aspiration for researchers. In this study, purified BNNT was used as a template and electrochemical support material for the nucleation of icosahedral palladium on its surface using an external surfactant and reductant-free solvothermal strategy. The developed IC-Pd@BNNT demonstrated excellent hydrogen evolution capabilities in 0.5 M H_2SO_4 with an overpotential of 15.7 mV at -20 mA cm^{-2}, higher than the commercial Pd/C (62.6 mV) and Pt/C (29.4 mV). The overpotential reached as low as 199 mV at a high current density (-1000 mA cm^{-2}), with excellent stability until 32% and high mass activity (620.31 A g$_{Pd}^{-1}$). The IC-Pd@BNNT catalysts show the ultralow

overpotential, which is much lower than that of most efficient electrocatalysts containing Pd with carbon support as well as other noble metals. DFT calculations show that the IC-Pd facet site on the defective BNNT support is highly active for the HER, and the V9-Pd_{13}-BN illustrated the best active and stable model. The IC-Pd@BNNT catalyst also exhibited high durability over 40000 cycles with zero reductions of overpotential and no structural damage even after 304 days in an acidic medium. The Faradaic efficiency was as high as 98.96%. Theoretically, it is shown that vacancies and C moieties in BNNTs readily enhance the ion mobility, conductivity of the catalysts. The newly designed IC-Pd@BNNT provides a novel platform for BNNT as a robust electrochemical catalytic support, as well as a template for in situ nucleation and growth of NPs. These attractive properties offer alternative options to carbon catalyst support that can improve the catalytic support systems in the energy sector.

CRediT authorship contribution statement

Kim Myung Jong: Conceptualization, Data curation, Formal analysis, Funding acquisition, Investigation, Methodology, Project administration, Resources, Supervision, Validation, Visualization, Writing – review & editing. **Han Sang Soo:** Data curation, Formal analysis, Funding acquisition, Investigation, Methodology, Project administration, Resources, Software, Supervision, Validation, Visualization, Writing – review & editing. **Yoon Minyoung:** Formal analysis, Supervision, Validation, Visualization, Writing – review & editing. **Nam Ki Tae:** Formal analysis, Resources. **Balamurugan Mani:** Data curation, Formal analysis, Resources, Validation. **Son Younghu:** Formal analysis. **Sada Venkateswarlu:** Conceptualization, Data curation, Formal analysis, Investigation, Methodology, Resources, Software, Validation, Visualization, Writing – original draft, Writing – review & editing. **Kim Sooyeon:** Data curation, Formal analysis, Investigation, Resources, Software, Validation, Visualization, Writing – original draft, Writing – review & editing.

Declaration of Competing Interest

The authors declare that they have no known competing financial interests or personal relationships that could have appeared to influence the work reported in this paper.

Data availability

Data will be made available on request.

Acknowledgements

Appendix A. Supplementary material

The following files are available free of charge. images, XPStion technique details, TEM, HRTE, HAADF-STEM line and elemental mapping images, EDS images, EPR spectrum, XPS, BET analysis data, contact angle images, Raman data with 3D mapping, FT-IR, TGA data, polarization curves normalized by ECSA and BET, EIS data of BNNT, H_2 gas

quantification chromatograms, various DFT structural models data, Post HAADF-STEM elemental mapping images, XPS, XRD spectrum, Tables S1-S8 and Videos S1, S2.

Supplementary data associated with this article can be found in the online version at doi:10.1016/j.apcatb.2023.123609.

References

[1] N.T. Suen, S.F. Hung, Q. Quan, N. Zhang, Y.J. Xu, H.M. Chen, Electrocatalysis for the oxygen evolution reaction: recent development and future perspectives, Chem. Soc. Rev. 46 (2017) 337–365, https://doi.org/10.1039/C6CS00328A.

[2] G. Palmer, Renewables rise above fossil fuels, Nat. Energy 4 (2019) 538–539, https://doi.org/10.1038/s41560-019-0426-y.

[3] Z. Li, Y. Feng, Y.L. Liang, C.Q. Cheng, C.K. Dong, H. Liu, X.W. Du, Stable rhodium (iv) oxide for alkaline hydrogen evolution reaction, Adv. Mater. 32 (2020), 1908521, https://doi.org/10.1002/adma.201908521.

[4] T. Kosmala, A. Baby, M. Lunardon, D. Perilli, H. Liu, C. Durante, C.D. Valentin, S. Agnoli, G. Granozzi, Operando visualization of the hydrogen evolution reaction with atomic-scale precision at different metal–graphene interfaces, Nat. Catal. 4 (2021) 850–859, https://doi.org/10.1038/s41929-021-00682-2.

[5] S. Liu, Y. Shen, Y. Zhang, B. Cui, S. Xi, J. Zhang, L. Xu, S. Zhu, Y. Chen, Y. Deng, W. Hu, Extreme environmental thermal shock induced dislocation-rich Pt nanoparticles boosting hydrogen evolution reaction, Adv. Mater. 34 (2022), 2106973, https://doi.org/10.1002/adma.202106973.

[6] J. Zhu, L. Hu, P. Zhao, L.Y.S. Lee, K.Y. Wong, Recent advances in electrocatalytic hydrogen evolution using nanoparticles, Chem. Rev. 120 (2020) 851–918, https://doi.org/10.1021/acs.chemrev.9b00248.

[7] S. Yang, Z. Si, G. Li, P. Zhan, C. Liu, L. Lu, B. Han, H. Xie, P. Qin, Single cobalt atoms immobilized on palladium-based nanosheets as 2D single-atom alloy for efficient hydrogen evolution reaction, Small 19 (2023), 2207651, https://doi.org/10.1002/smll.202207651.

[8] M. Iqbal, Y.V. Kaneti, J. Kim, B. Yuliarto, Y.M. Kang, Y. Bando, Y. Sugahara, Y. Yamauchi, Chemical design of palladium-based nanoarchitectures for catalytic applications, Small 15 (2019), 1804378, https://doi.org/10.1002/smll.201804378.

[9] A. Zalineeva, S. Baranton, C. Coutanceau, G. Jerkiewicz, Octahedral palladium nanoparticles as excellent hosts for electrochemically adsorbed and absorbed hydrogen, Sci. Adv. 3 (2017), e1600542, https://doi.org/10.1126/sciadv.1600542.

[10] H. Wang, S. Zhou, K.D. Gilroy, Z. Cai, Y. Xi, Icosahedral nanocrystals of noble metals: synthesis and applications, Nano Today 15 (2017) 121–144, https://doi.org/10.1016/j.nantod.2017.06.011.

[11] A. Oh, H.Y. Kim, H. Baik, B. Kim, N.K. Chaudhari, S.H. Joo, K. Lee, Topotactic transformations in an icosahedral nanocrystal to form efficient water-splitting catalysts, Adv. Mater. 31 (2019), 1805546, https://doi.org/10.1002/adma.201805546.

[12] S.C. Hsu, Y.C. Chuang, B.T. Sneed, D.A. Cullen, T.W. Chiu, C.H. Kuo, turning the halide switch in the synthesis of Au-Pd alloy and core–shell nano icosahedra with terraced shells: performance in electrochemical and plasmon-enhanced catalysis, Nano Lett. 16 (2016) 5514–5520, https://doi.org/10.1021/acs.nanolett.6b02005.

[13] X. Li, X. Li, C. Liu, H. Huang, P. Gao, F. Ahmad, L. Luo, Y. Ye, Z. Geng, G. Wang, R. Si, C. Ma, J. Yang, J. Zeng, Atomic-level construction of tensile-strained PdFe alloy surface toward highly efficient oxygen reduction electrocatalysis, Nano Lett. 20 (2020) 1403–1409, https://doi.org/10.1021/acs.nanolett.9b05024.

[14] Y. Feng, Q. Shao, Y. Ji, X. Cui, Y. Li, X. Zhu, X. Huang, Surface-modulated palladium- nickel icosahedra as high-performance non-platinum oxygen reduction electrocatalysts, Sci. Adv. 4 (2018), eaap8817, https://doi.org/10.1126/sciadv.aap8817.

[15] Z. Lyu, S. Zhu, L. Xu, Z. Chen, Y. Zhang, M. Xie, T. Li, S. Zhou, J. Liu, M. Chi, M. Shao, M. Mavrikakis, Y. Xia, Kinetically controlled synthesis of Pd-Cu Janus nanocrystals with enriched surface structures and enhanced catalytic activities toward CO₂ reduction, J. Am. Chem. Soc. 143 (2021) 149–162, https://doi.org/10.1021/jacs.0c05408.

[16] M. Liu, Z. Lyu, Y. Zhang, R. Chen, M. Xie, Y. Xia, Twin-directed deposition of Pt on Pd icosahedral nanocrystals for catalysts with enhanced activity and durability toward oxygen reduction, Nano Lett. 21 (2021) 2248–2254, https://doi.org/10.1021/acs.nanolett.1c00007.

[17] H. Huang, M. Yan, C. Yang, H. He, Q. Jiang, L. Yang, Z. Lu, Z. Sun, X. Xu, Y. Bando, Y. Yamauchi, Graphene nanoarchitectonics: recent advances in graphene-based electrocatalysts for hydrogen evolution reaction, Adv. Mater. 31 (2019), 1903415, https://doi.org/10.1002/adma.201903415.

[18] R. Arrigo, M.E. Schuster, Z. Xie, Y. Yi, G. Wowsnick, L.L. Sun, K.E. Hermann, M. Friedrich, P. Kast, M. Havecker, A.K. Gericke, R. Schlogl, Nature of the N–Pd interaction in nitrogen-doped carbon nanotube catalysts, ACS Catal. 5 (2015) 2740–2753, https://doi.org/10.1021/acscatal.5b00094.

[19] G. Valenti, A. Boni, M. Melchionna, M. Cargnello, L. Nasi, G. Bertoni, R.J. Gorte, M. Marcaccio, S. Rapino, M. Bonchio, P. Fornasiero, M. Prato, F. Paolucci, Co-axial heterostructures integrating palladium/titanium dioxide with carbon nanotubes for efficient electrocatalytic hydrogen evolution, Nat. Comm. 7 (2017), 13549, https://doi.org/10.1038/ncomms13549.

[20] D.S. Butenko, S. Li, V.O. Kotsyubynsky, V.M. Boychuk, V.I. Dubinko, P. I. Kolkovsky, N.A. Liedienov, N.I. Klyui, W. Han, I.V. Zatovsky, Palladium nanoparticles embedded in microporous carbon as electrocatalysts for water

[21] splitting in alkaline media, Int. J. Hydrog. Energy 46 (2021), 214624, https://doi.org/10.1016/j.ijhydene.2021.03.242.

[22] Y.S. Horn, W.C. Sheng, S. Chen, P.J. Ferreira, E.F. Holby, D. Morgan, Instability of supported platinum nanoparticles in low-temperature fuel cells, Top. Catal. 46 (2007) 285, https://doi.org/10.1007/s11244-007-9000-0.

[22] A. Chalgin, C. Song, P. Tao, W. Shang, T. Deng, J. Wu, Effect of supporting materials on the electrocatalytic activity, stability and selectivity of noble metal-based catalysts for oxygen reduction and hydrogen evolution reactions, Prog. Nat. Sci. 30 (2020) 289–297, https://doi.org/10.1016/j.pnsc.2020.01.003.

[23] T. Bhowmik, M.K. Kundu, S. Barman, Palladium nanoparticle−graphitic carbon nitride porous synergistic catalyst for hydrogen evolution/oxidation reactions over a broad range of pH and correlation of its catalytic activity with measured hydrogen binding energy, ACS Catal. 6 (2016) 1929–1941, https://doi.org/10.1021/acscatal.5b02485.

[24] C. Zhi, Y. Bando, C. Tang, D. Golberg, Boron nitride nanotubes, Mater. Sci. Eng. R. 70 (2010) 92–111, https://doi.org/10.1016/j.mser.2010.06.004.

[25] J.H. Kim, T.V. Pham, J.H. Hwang, C.S. Kim, M.J. Kim, Boron nitride nanotubes: synthesis and applications, Nano Converg. 5 (2018) 1–13, https://doi.org/10.1186/s40580-018-0149-y.

[26] S. Li, L. Ci, H. Lu, P.B. Sorokin, C. Jin, J. Ni, A.G. Kvashnin, D.G. Kvashnin, J. Lou, B.I. Yakobson, P.M. Ajayan, Large scale growth and characterization of atomic hexagonal boron nitride layers, Nano Lett. 10 (2010) 3209–3215, https://doi.org/10.1021/nl1022139.

[27] N.G. Chopra, R.J. Luyken, K. Cherrey, V.H. Crespi, M.L. Cohen, S.G. Louie, A. Zettl, Boron nitride nanotubes, Science 269 (1995) 966–967, https://doi.org/10.1126/science.269.5226.966.

[28] H. Liu, X.H. Zhang, Y.X. Li, X. Li, C.K. Dong, D.Y. Wu, C.C. Tang, S.L. Chou, F. Fang, X.W. Du, Conductive boron nitride as promising catalyst support for the oxygen evolution reaction, Adv. Energy Mater. 10 (2020), 1902521, https://doi.org/10.1002/aenm.201902521.

[29] Y. Chen, J. Cai, P. Li, G. Zhao, G. Wang, Y. Jiang, J. Chen, S.X. Dou, H. Pan, W. Sun, Hexagonal Boron nitride as a multifunctional support for engineering efficient electrocatalysts toward the oxygen reduction reaction, Nano Lett. 20 (2020) 6807, https://doi.org/10.1021/acs.nanolett.0c02782.

[30] L. Chen, L.R. Zhang, L.Y. Yao, Y.H. Fang, L. He, G.F. Wei, Z.P. Liu, Metal boride better than Pt: HCP Pd2B as a superactive hydrogen evolution reaction catalyst, Energy Environ. Sci. 12 (2019) 3099–3105, https://doi.org/10.1039/C9EE01564G.

[31] J. Wu, M.T.F. Rodrigues, R. Vajtai, P.M. Ajayan, Tuning the electrochemical reactivity of boron- and nitrogen-substituted graphene, Adv. Mater. 28 (2016) 6239–6246, https://doi.org/10.1002/adma.201506316.

[32] D.Q. Liu, B. Tao, H.C. Ruan, C.L. Bentley, P.R. Unwin, Metal support effects in electrocatalysis at hexagonal boron nitride, Chem. Commun. 55 (2019) 628–631, https://doi.org/10.1039/C8CC08517J.

[33] S. Anantharaj, S.R. Ede, K. Karthick, S. Sam Sankar, K. Sangeetha, P.E. Karthik, S. Kundu, Precision and correctness in the evaluation of electrocatalytic water splitting: revisiting activity parameters with a critical assessment, Energy Environ. Sci. 11 (2018) 744–771, https://doi.org/10.1039/C7EE03457A.

[34] A.M. Harzandi, S. Shadman, M. Ha, C.W. Myung, D.Y. Kim, H.J. Park, S. Sultan, W. S. Noh, W. Lee, P. Thangavel, W.J. Byun, S.H. Lee, J.N. Tiwari, T.J. Shin, J.H. Park, Z. Lee, J.S. Lee, K.S. Kim, Immiscible bi-metal single-atoms driven synthesis of electrocatalysts having superb mass-activity and durability, Appl. Catal. B: Environ. 270 (2020), 118896, https://doi.org/10.1016/j.apcatb.2020.118896.

[35] N.K. Dang, J.N. Tiwari, S. Sultan, A. Meena, K.S. Kim, Multi-site catalyst derived from Cr atoms-substituted CoFe nanoparticles for high-performance oxygen evolution activity, Chem. Eng. J. 404 (2021) 126513, https://doi.org/10.1016/j.cej.2020.126513.

[36] G. Kresse, J. Furthmuller, Efficient iterative schemes for ab initio total-energy calculations using a plane-wave basis set, Phys. Rev. B 54 (1996) 11169–11186, https://doi.org/10.1103/PhysRevB.54.11169.

[37] G. Kresse, J. Hafner, Ab initio molecular-dynamics simulation of the liquid-metal–amorphous-semiconductor transition in germanium, Phys. Rev. B 49 (1994) 14251–14269, https://doi.org/10.1103/PhysRevB.49.14251.

[38] P.E. Blochl, Projector augmented-wave method, Phys. Rev. B 50 (1994) 17953–17979, https://doi.org/10.1103/PhysRevB.50.17953.

[39] B. Hammer, L.B. Hansen, J.K. Nørskov, Improved adsorption energetics within density- functional theory using revised Perdew-Burke-Ernzerhof functionals, Phys. Rev. B 59 (1999) 7413–7421, https://doi.org/10.1103/PhysRevB.59.7413.

[40] S. Grimme, J. Antony, S. Ehrlich, H. Krieg, A consistent and accurate ab initio parametrization of density functional dispersion correction (DFT-D) for the 94 elements H-Pu, J. Chem. Phys. 132 (2010), 154104, https://doi.org/10.1063/1.3382344.

[41] P. Su, W. Pei, X. Wang, Y. Ma, Q. Jiang, J. Liang, S. Zhou, J. Zhao, J. Liu, G.Q. Lu, Exceptional electrochemical HER performance with enhanced electron transfer between Ru nanoparticles and Single atoms dispersed on a carbon substrate, Angew. Chem. Int. Ed. 60 (2021) 16044, https://doi.org/10.1002/anie.202103557.

[42] M. Vyas, F. Fajardo-Rojas, D.A. Gómez-Gualdron, S. Kwon, Theoretical assessments of Pd–PdO phase transformation and its impacts on H2O2 synthesis and decomposition pathways, Catal. Sci. Technol. 13 (2023) 3828–3848, https://doi.org/10.1039/D3CY00404J.

[43] J.K. Nørskov, J. Rossmeisl, A. Logadottir, L. Lindqvist, J.R. Kitchin, T. Bligaard, H. Jonsson, Origin of the overpotential for oxygen reduction at a fuel-cell cathode, J. Phys. Chem. B 108 (2004) 17886–17892, https://doi.org/10.1021/jp047349j.

[44] J.K. Norskov, T. Bligaard, A. Logadottir, J.R. Kitchin, J.G. Chen, S. Pandelov, U. Stimming, Trends in the exchange current for hydrogen evolution, J. Electrochem. Soc. 152 (2005) J23–J26, https://doi.org/10.1149/1.1856988.

[45] T. Nagata, Y. Obora, N, N-Dimethylformamide-protected single-sized metal nanoparticles and their use as catalysts for organic transformations, ACS Omega 5 (2020) 98–103, https://doi.org/10.1021/acsomega.9b03828.

[46] C. Li, R. Sato, M. Kanehara, H. Zeng, Y. Bando, T. Teranishi, Controllable polyol synthesis of uniform palladium icosahedra: effect of twinned structure on deformation of crystalline lattices, Angew. Chem. Int. Ed. 48 (2009) 6883–6887, https://doi.org/10.1002/anie.200902786.

[47] S. Zhou, C. Wang, Y. Xia, Controllable polyol synthesis of uniform palladium icosahedra: effect of twinned structure on deformation of crystalline lattices, Chem. Mater. 34 (2022) 5065–5073, https://doi.org/10.1021/acs.chemmater.2c00397.

[48] X. Wang, L.F. Cosme, X. Yang, M. Luo, J. Liu, Z. Xie, Y. Xia, Pt-based icosahedral nanocages: using a combination of {111} facets, twin defects, and ultrathin walls to greatly enhance their activity toward oxygen reduction, Nano Lett. 16 (2016) 1467–1471, https://doi.org/10.1021/acs.nanolett.5b05140.

[49] R. Schimmenti, R. Cortese, F. Ferrante, A. Prestianni, D. Duca, Growth of sub-nanometric palladium clusters on boron nitride nanotubes: a DFT study, Phys. Chem. Chem. Phys. 18 (2016) 1750–1757, https://doi.org/10.1039/C5CP06625E.

[50] G.A.A. Monteiro, R.G. Sousa, W.M. Silva, P.L. Gastelois, W.A.A. Macedo, E.M. B. Sousa, Microwave radiation-assisted covalent functionalization of boron nitride nanotubes and their grafting with cationic thermos and pH-sensitive hydrogel, Appl. Nanosci. 11 (2021) 505–520, https://doi.org/10.1007/s13204-020-01610-9.

[51] M.S. Amin, T.E. Molin, C. Tampubolon, D.E. Kranbuehl, H.C. Schniepp, Boron nitride nanotube impurity detection and purity verification, Chem. Mater. 32 (2020) 9090–9097, https://doi.org/10.1021/acs.chemmater.0c03609.

[52] R. Liu, Z. Gong, J. Liu, J. Dong, J. Liao, H. Liu, H. Huang, J. Liu, M. Yan, K. Huang, H. Gong, J. Zhu, C. Cui, G. Ye, H. Fei, Design of Aligned Porous Carbon Films with Single Atom Co–N–C Sites for High-Current-Density Hydrogen Generation, Adv. Mater. 14 (2021), 2103533, https://doi.org/10.1002/adma.202103533.

[53] J. Mahmood, M.A.R. Anjum, S.H. Shin, I. Ahmad, H.J. Noh, S.J. Kim, H.Y. Jeong, J. S. Lee, J.B. Baek, Encapsulating Iridium Nanoparticles Inside a 3D Cage-Like Organic Network as an Efficient and Durable Catalyst for the Hydrogen Evolution Reaction, Adv. Mater. 30 (2018), 1805606, https://doi.org/10.1002/adma.201805606.

[54] B. Hammer, J.K. Nørskov, Why gold is the noblest of all the metals, Nature 376 (1995) 238–240, https://doi.org/10.1038/376238a0.

[55] J.K. Norskov, F. Abild-Pedersen, F. Studt, T. Bligaard, Density functional theory in surface chemistry and catalysis (USA), P. Natl. Acad. Sci. 108 (2011) 937–943, https://doi.org/10.1073/pnas.1006652108.

[56] C.Q. Ma, Y.L. Zhang, S.H. Yan, B.P. Liu, Carbon-doped boron nitride nanosheets: a high-efficient electrocatalyst for ambient nitrogen reduction, 315, Appl. Catal. B-Environ. 315 (2022) 121574, https://doi.org/10.1016/j.apcatb.2022.121574.

[57] M. Chhetri, S. Maitra, H. Chakraborty, U.V. Waghmare, C.N.R. Rao, Superior performance of borocarbonitrides, BxCyNz, as stable, low-cost metal-free electrocatalysts for the hydrogen evolution reaction, Environ. Sci. 9 (2016) 95–101, https://doi.org/10.1039/C5EE02521D.